Target Motion Discrimination with Model Retina and Cortex

by

Maha A. P. Neshadha Perera, B.S.

A Thesis

in

Mathematics

Submitted to the Graduate Faculty
of Texas Tech University in
Partial Fulfillment of
the Requirements for the Degree of

Master of Science

Approved

Dr. Bijoy K. Ghosh
Chair of Committee

Dr. Clyde F. Martin

Peggy Gordon Miller
Interim Dean of the Graduate School

August, 2011

ACKNOWLEDGMENTS

First and foremost, I would like to express my heartfelt gratitude to my advisor Dr. Bijoy K. Ghosh for his invaluable guidance and support, both academically and morally given to me while I was working on this project. Without the knowledge, encouragement, and fatherly advice given by you, this project could have been much more difficult and less productive.

I must also thank my thesis committee member Dr. Clyde F. Martin for the support given even with his busy schedule. Your presence in my thesis committee, and your corporation is highly appreciated.

If I don't mention the support given by my colleague Mervyn Parakrama Ekanayaka for completing this thesis, it would be an extremely ungrateful thing. Being a fellow researcher in my research group and a good friend, his valuable support made my life much easier. I would like to thank Mervyn from the bottom of my heart.

Another big chunk of my thanks goes to my loving wife Kalpana who took care of me tirelessly while I am working on this research project.

Last but not least, I would like to thank everyone else who supported me during my stay in Texas Tech University in various instances. Even though I could not name everyone individually, I would like to express my heartfelt gratitude to all of you.

CONTENTS

ABSTRACT

A model of a turtle's visual cortex has been developed and successfully used to discriminate different input stimuli to different locations of its lateral geniculate nucleus. The turtle's retina model also shows the capability of discriminating motion targets which verifies the biological experimental results. However, the two models are studied separately and have been driven by different input stimuli in the past. Here, in this thesis we will be combining the two models and let the output of the retinal model drive the visual cortex model. We will be paying attention to the model parameters such as the connection strength between the two previous models and the white noise levels during this experiment.

LIST OF FIGURES

CHAPTER I
INTRODUCTION

The visual system of freshwater turtles consist of three major components which have been studied in detail. The turtle retina on which an image is formed within an eye has been studied and a detailed model was derived. The visual cortex, which is a part of the turtle's brain where the optical nerve connects also has been studied and a detailed model was derived. Both models have shown promising results when working alone for simulated data.

In this thesis, an attempt has made to combine the two models through a simple model of Lateral Geniculate Nucleus (LGN). The simulation of motion targets of different angles was performed with the combined model.

This thesis consists of the following chapters which describe the biological model of the turtle's visual system, simulation model of the turtle's visual system and simulation parameters.

The first chapter, Biology of the Turtle Visual System describes the each major component of interest in the Turtle's visual system. The retina, which is a part of the Turtle's eye, the Visual cortex which is a part of the Turtle' brain and the Lateral Geniculate Complex (LGN) which connects the retina to the Turtle's Visual cortex is described in this chapter.

The next chapter describes the model used to simulate the Turtle visual system which contains GENESIS models of retina and Visual cortex, and the linear model of LGN. This chapter also describes the parameters of the model which has been tweaked during the simulation study to determine the characteristics of the complete model.

The final chapter describes the simulation results and the interpretations of the results observed. It also describes methods which can be used to discriminate the motions targets using the Visual Cortex activities.

CHAPTER II
BIOLOGY OF THE TURTLE VISUAL SYSTEM

Here we analyze the visual system of freshwater turtles. The freshwater turtle visual system is similar to that of most vertebrates. In fact, all vertebrate retina share a similar structure (See [2] and [14]). Therefore, a turtle being a vertebrate can be used to study the vertebrate visual system. Furthermore, the structure of the turtle visual system has been extensively studied and detailed models were developed and successfully tested at the Center for Bio Cybernetics and Intelligent Systems at Texas tech University and various other research centers and laboratories around the world.

A general discussion of the cerebral cortex of reptiles,including turtles is provided in [18] , and a detailed discussion of the visual pathways in turtles is provided in [19]. Nenadic *et al.* in [9] provides a large scale model of the visual cortex.

Neuronal activities in the turtle's visual system have been studied using different methods. Some of these methods are, recording from external surface of the brain using multi-electrode arrays [11], [12], imaging the external surface of the cortex with voltage-sensitive dyes, [13] and imaging the ependymal surface of the cortex with voltage-sensitive dyes [15], [16], [17] and [10].

The following figure (Figure 2.1) shows the complete visual system of a freshwater turtle. The turtle's eyes, brain and optical nerve can be seen clearly in this picture. CTX: cortex, OT: optic tectum and CB: cerebellum are also shown in the figure.

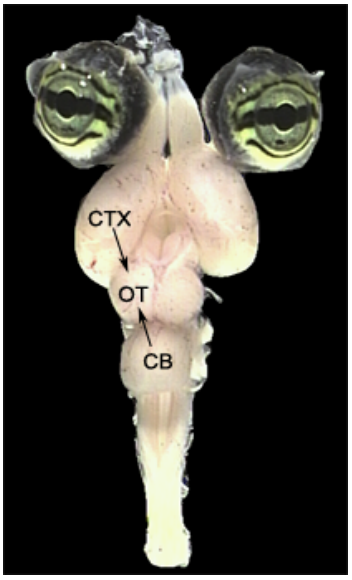

Figure 2.1: Complete Turtle Visual System *Picture courtesy of David M. Senseman, University of Texas at San Antonio, San Antonio, TX*

2.1 Neurons

The building block of any vertebrate visual system is a neuron. Neurons are elongated cells which make up the central nervous system and they carry messages by means of electrical signals.

The figure 2.2 below shows a typical neuron consists of dendrites, a cell body known as soma and an axon. The cell body contains the nucleus and controls the metabolic activities of the cell. The axon is the nerve fiber which transmits the impulses away from the cell body. The myelin sheath acts as an insulator and allow neurons to transmit the impulses faster. These axons end as swellings known as synaptic terminals. When exited, neurotransmitters are released from these synaptic terminals into the synapse which is the gap between a synaptic terminal of one cell and the dendrite of the adjacent cell. The dendrites act as signal receptors from the axon terminals of other neurons.

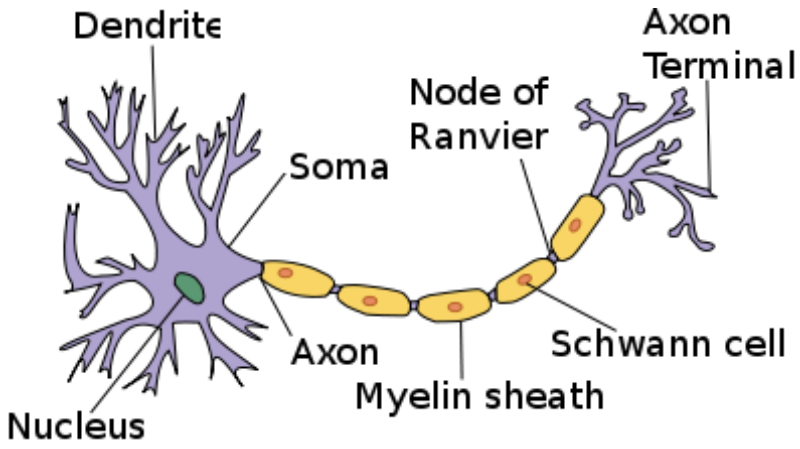

Figure 2.2: Structure of a typical neuron *Copylefted image attributed to Quasar Jarosz at* `en.wikipedia`.

The potential of the cell membrane of each neuron is measured as the activity level of that particular neuron. The membrane potential level creates spikes when it exceeds a certain threshold level and these spikes causes a neural signal to be passed from one neuron to the other by releasing neurotransmitters at synaptic terminals.

2.2 The Retina

All vertebrate retina share a similar structure (See [2] and [14]). It consist of layers of cells which are located inside the eye. The image of what eye sees is formed on the retina. The cells in the retina are specialized to encode visual information efficiently.

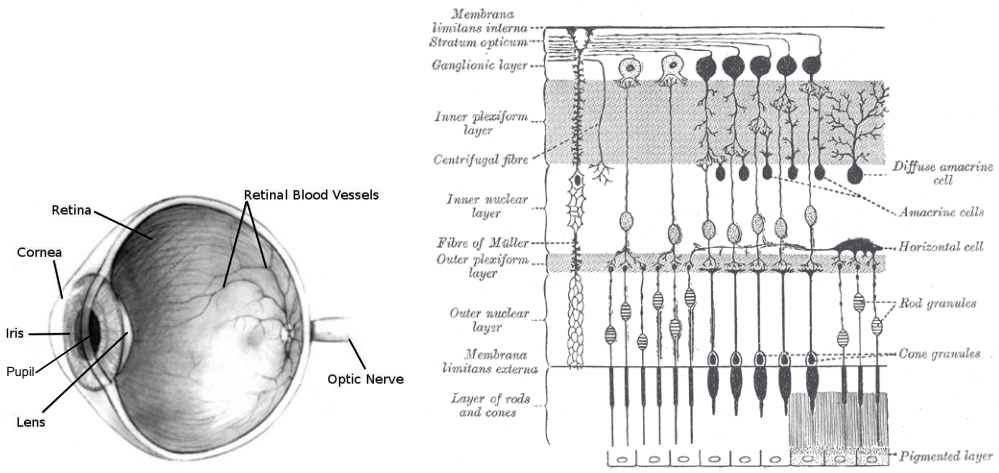

(a) Vertebrate Eye (b) Vertebrate Retina

Figure 2.3: Vertebrate eyes and retina. (a) Cross section of the eye of an vertebrate *Copyright: public domain - credit to NIH National Eye Institute.* (b) Layered structure of the vertebrate retina *Copyright: public domain - copyright expired.*

Light travels through the transparent ganglion cell layers and fall on the rods and cone cells. The rod and cone cells are sensitive to light and get excited when light falls on them. The signals generated by these rods and cones are then transfered to the retinal ganglion cells which makes the optical nerve and travels towards deeper structures of the brain.

There are two basic types of ganglion cells which we are interested in the turtle's retina known as A-cells and B-cells. They are classified based on their directional sensitivity.

2.3 Visual Cortex & LGN

The Lateral Geniculate Nucleus (LGN) connects the optic nerve coming from the retina into the visual cortex in the brain. The visual cortex is located in the brain and it plays a major role in decoding the signals coming from the retina.

Turtle's visual cortex and Lateral Geniculate Nucleus (LGN) are shown in figure 2.4 below. The figure shows the following components:

A : Dorsal view of a turtle brain. The oval-shaped area represents the visual cortex,

which corresponds to the dorsal area, D. OB, olfactory bulb; CTX, cortex; OT, optic tectum; CB, cerebellum.

B : Coronal section through the cerebral cortex at the level indicated in A. ADVR, anterior dorsal ventricular ridge; STR, striatum; D_M, medial part of D; D_L, lateral part of D.

C : Detailed view of visual cortex showing a medial and lateral pyramidal cell

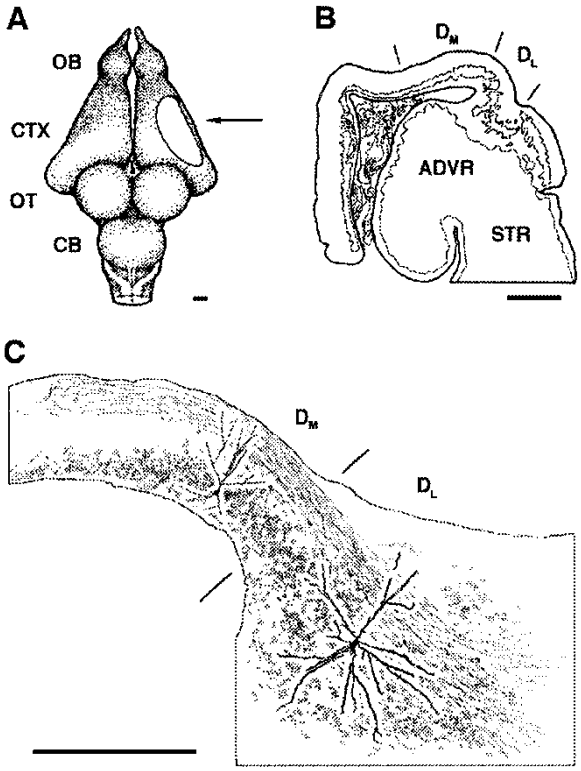

Figure 2.4: Turtle Visual Cortex. *Courtesy of the Ulinski lab at the University of Chicago.*

CHAPTER III
THE SIMULATION MODEL

The retina and visual cortex models developed at the Center for Bio Informatics & Cybernetics were using Hodgkin-Huxley model [5] to simulate neurons in these models.

However, the portion of the retinal consist of photo receptor cell layers was simulated using Matlab as a series of filters (See [4] for more details). Excitatory and inhibitory conductance responses were generated for each motion path simulated and used for simulating the retina model consists of retinal ganglion cells using the GENESIS neural simulator. The ganglion cells of the retina are connected to the visual cortex cells via a linear LGN structure.

3.1 GENESIS Model

Only a central patch of the actual turtle's retina was modeled using the GENESIS neural simulator. The cell distribution of the complete retina is illustrated in the figure 3.1.

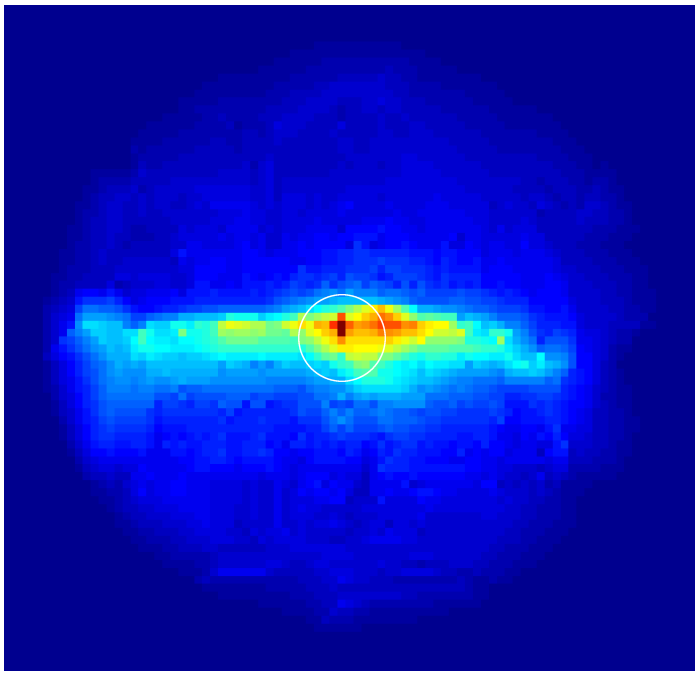

Figure 3.1: Cell distribution of the retina and the selected retinal patch
Cell distribution of the retina and the selected retinal patch. *Picture courtesy of Mervyn P. B. Ekanayaka, Center for Bio Cybernetics & Intelligent Systems at Texas Tech University, Lubbock, TX*

The white circle in the center shows the patch of the retina used in this simulation. Even though the actual retina contains nearly 400,000 cells, the selected retinal patch has only 520 cells. The only reason for selecting a smaller patch instead of the complete retina is the limitation of computational power.

There are two main categories of retinal cells simulated in this study. They are called A-cells and B-cells. A Cells are direction insensitive while B cells are direction sensitive. A cells can be further classified as A ON cells and A OFF cells and B cells can be classified as B1, B2 and B3 cells based on their direction sensitivity [1] . The figure 3.2 shows the distribution of these cells within the selected retinal patch.

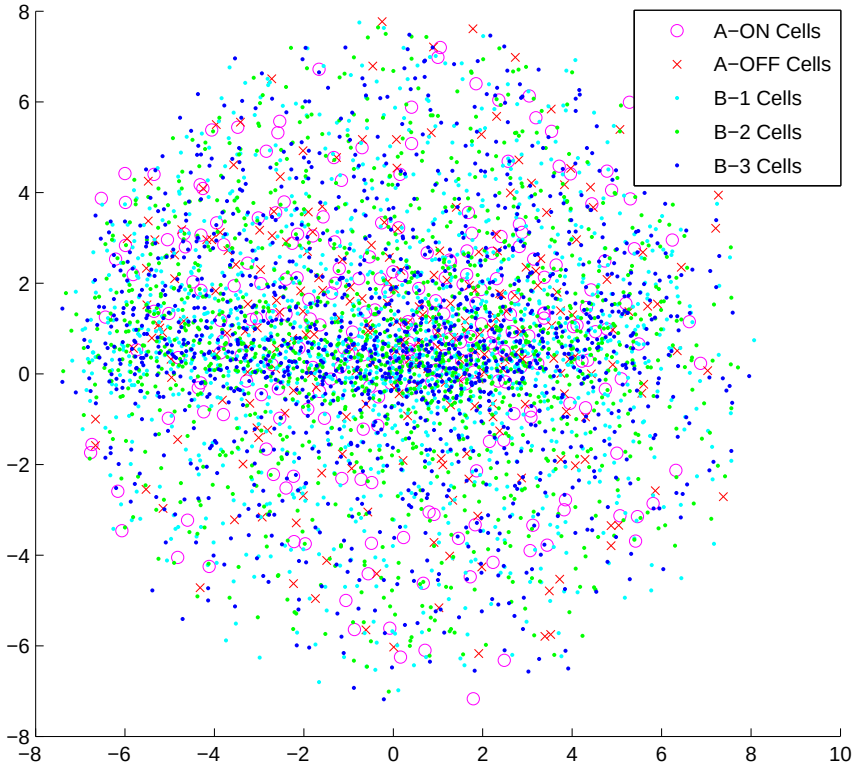

Figure 3.2: Ganglion cell distribution of the selected retinal patch

The large scale model of the visual cortex used in this simulation is based on the biological model described in [18] and [19]. This model has been developed into a computer model in [7], [8] and [9]. There are four major types of neurons in the visual cortex which we are interested in modeling. They are lateral pyramidal cells, medial pyramidal cells, stellate cells and horizontal cells. Each of these cell types and their corresponding connections with other cells are illustrated in figure 3.3

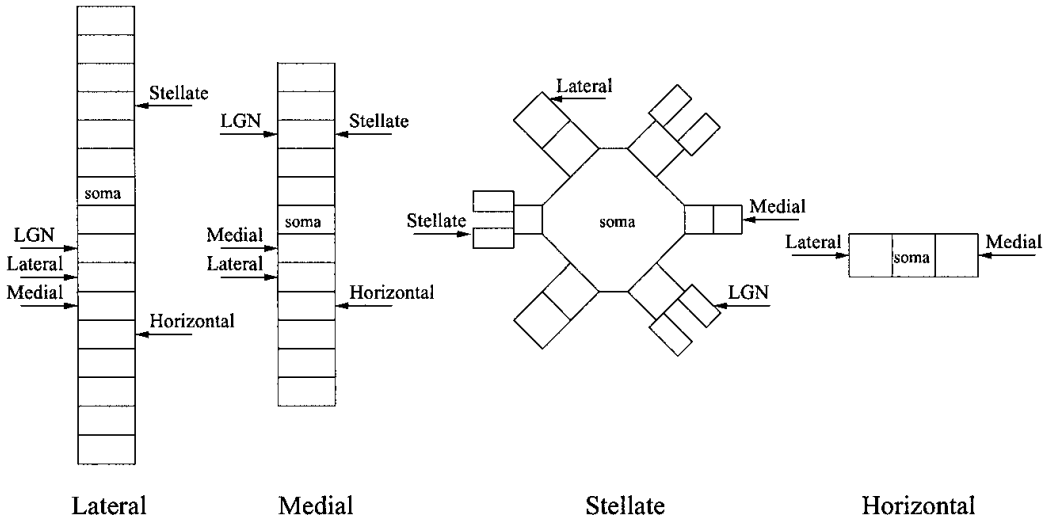

Figure 3.3: Types of neurons in visual cortex

The cell distribution within the visual cortex as described in [7], [8] and [9] is shown in figure 3.4. A linear LGN with 200 cells is also shown in black at the bottom right corner in this figure.

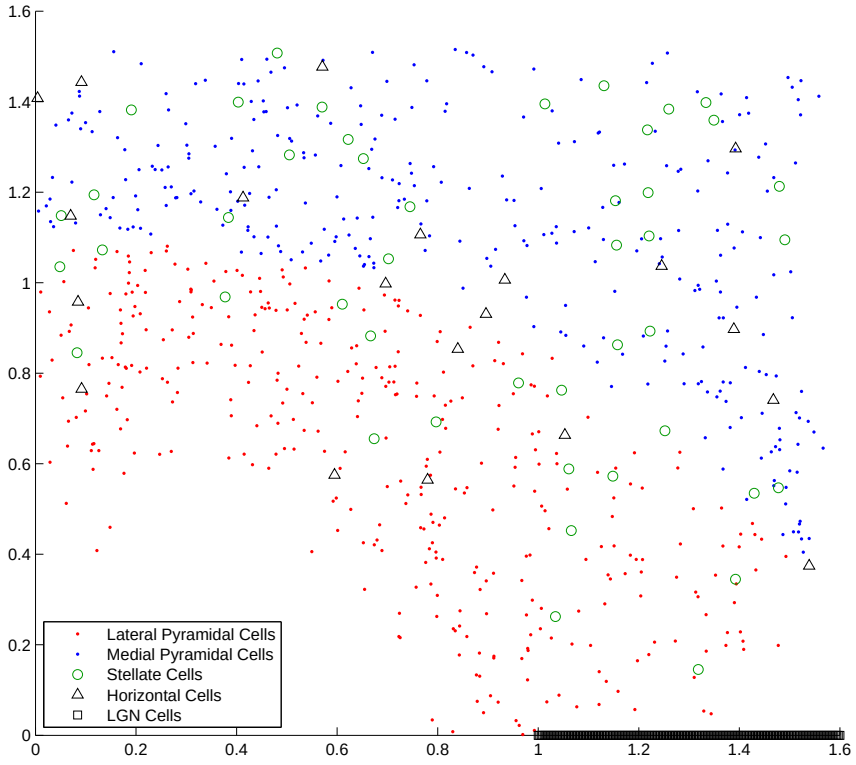

Figure 3.4: Cell distribution of the Visual Cortex

The linear arrangement of Lateral Geniculate Neurons are shown in figure 3.5. Only 13 such neurons are shown here for the clarity of the figure. However, in the actual simulation model, there are 200 geniculate neurons present.

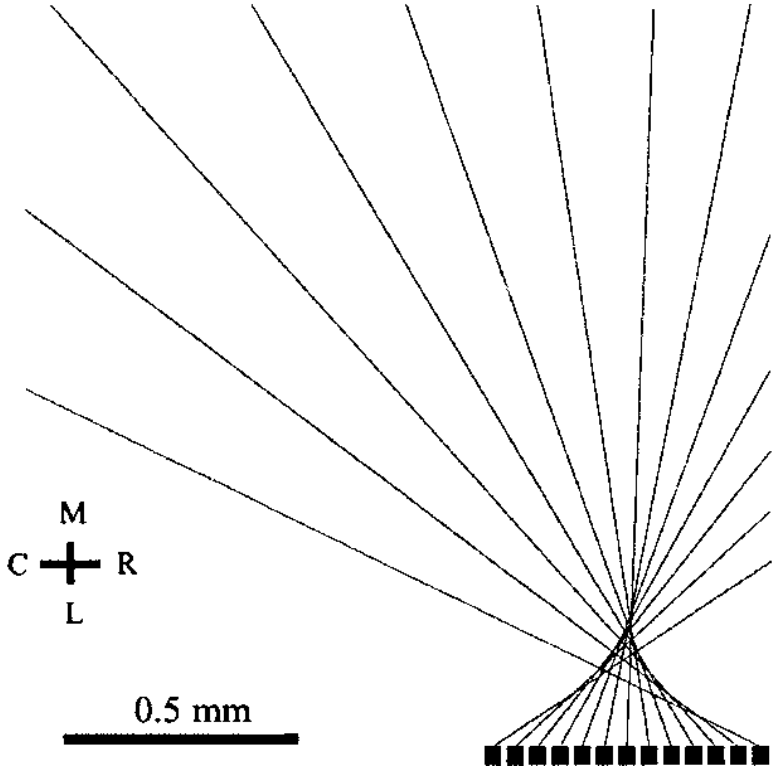

Figure 3.5: Linear arrangement of geniculate neurons

The two models were connected using a linear topology. The ganglion cells in the retinal model are grouped into 200 groups uniformly based on their x-coordinate. Each ganglion cell in the first group was connected to the first LGN cell using synapses, second group was connected to the second LGN cell and this pattern continued until all ganglion cells were connected into the LGN cells.

However, when creating the synapses, a synaptic delay was introduced based on the distance to each ganglion cell from the x-axis. Ganglion cells lie on x-axis connects to the LGN with zero delay while ganglion cells lies farthest away from x-axis connects to the LGN with the highest delay. The connection topology is illustrated in figure 3.6

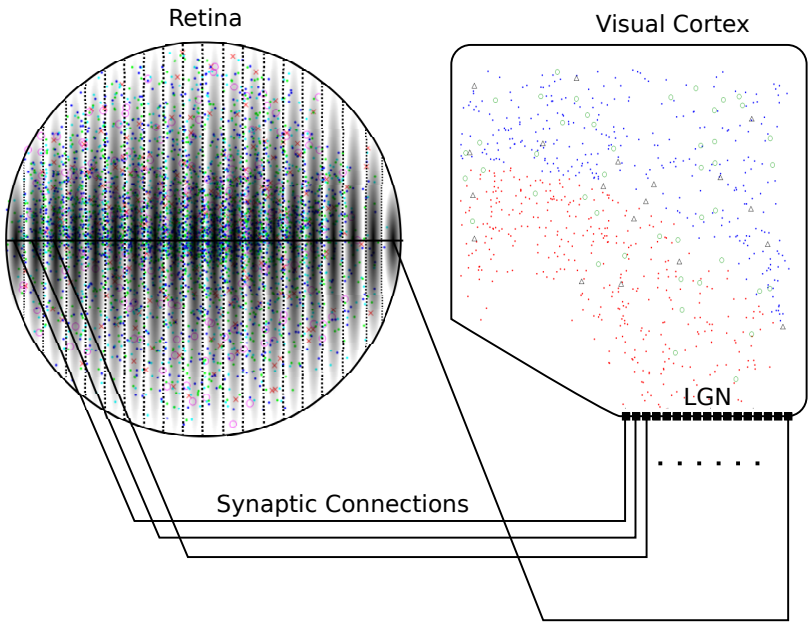

Figure 3.6: Retina and visual cortex combined model

3.2 Connection Strength

The connection strength between retinal model and the visual cortex model was found using a series of simulations run with connection strengths ranging from 0.1 to 10. The optimum connection strength was selected by visually observing the movies obtained from the visual cortex activity levels recorded in each simulation. A Connection strength of 1.0 was finally selected as the best connection strength for this particular series of simulations.

However, when the models were connected using any significant connection strengths from the beginning of the simulation time, i.e t = 0ms, a uniform activity pattern in the visual cortex was observed regardless of the input stimuli to the retinal model as shown in the figure 3.7a. The retinal model takes some time to stabilize and until then it produce random spikes causing the behavior observed.

As a remedy to this problem, the connection strength was dynamically changed during the simulation. Here the simulation was started with connection strength of 0 and it was changed to the desired connection strength of 1.0 after 100ms of simulation elapsed.

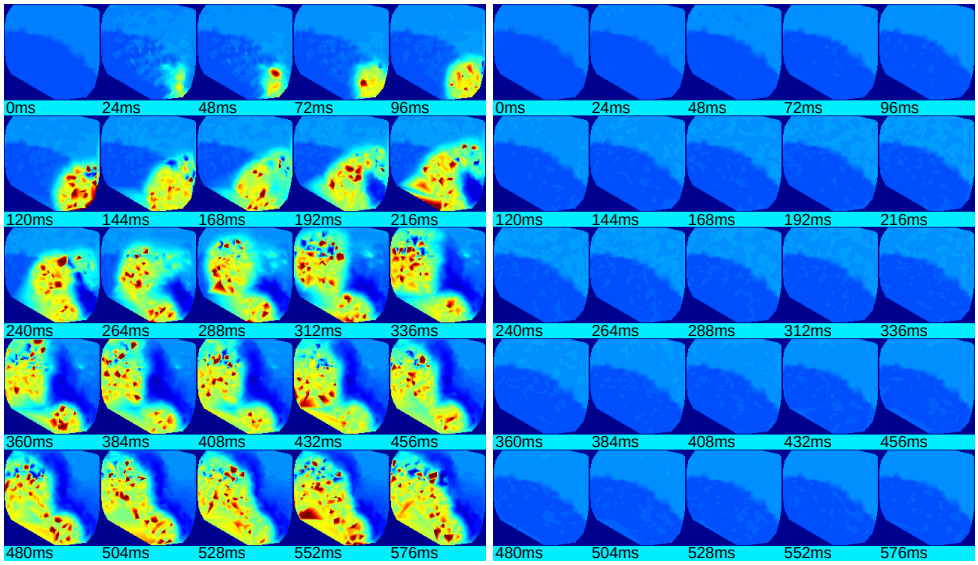

(a) With Static Connection Weights (b) With Dynamic Connection Weights

Figure 3.7: Cortical response movie with no input signal to retina

3.3 Visual Cortex Noise Level

For the purpose of statistical analysis, a Gaussian white noise was added to the visual cortex ganglion cells. Four different levels of white noise was tested (See figure 3.8) and finally white noise from a Gaussian distribution with $\mu = 0V$ and $\sigma^2 = 3.0 \times 10^{-10}V^2$ was selected (See figure 3.8c) in this simulation. Since the simulation was repeated 60 times per each motion target, this white noise allows us to analyze the data with statistical methods described in [3] and [8]

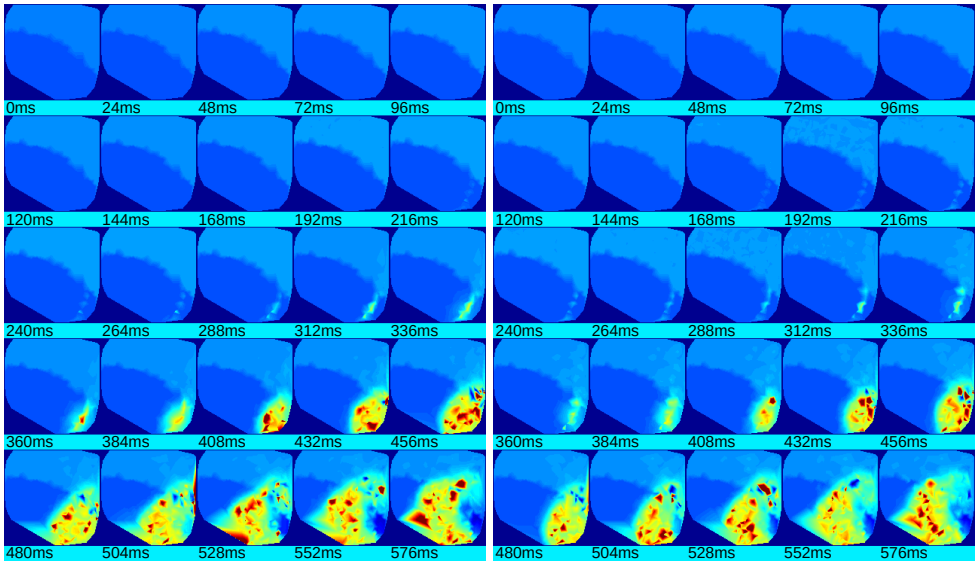

(a) $\mu = 0\ V$ and $\sigma^2 = 3.0 \times 10^{-12}\ V^2$ (b) $\mu = 0\ V$ and $\sigma^2 = 3.0 \times 10^{-11}\ V^2$

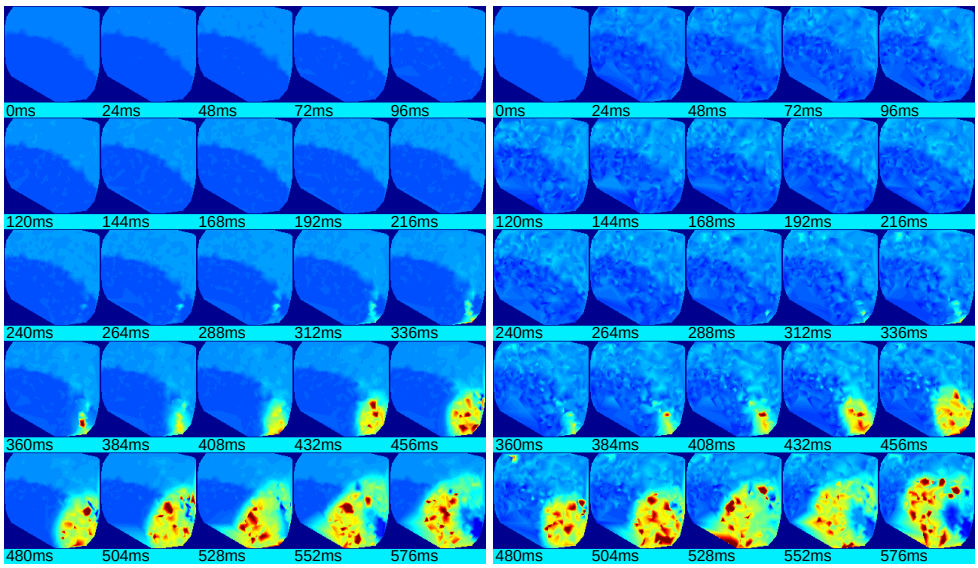

(c) $\mu = 0\ V$ and $\sigma^2 = 3.0 \times 10^{-10}\ V^2$ (d) $\mu = 0\ V$ and $\sigma^2 = 3.0 \times 10^{-9}\ V^2$

Figure 3.8: Cortical response movies for different white noise levels

CHAPTER IV
SIMULATION RESULTS

The Visual Cortex action potentials or the cortical responses were recorded for each neuron in the visual cortex for 1500ms time interval. Simulation was repeated 60 times per one motion path and total of twelve motion paths corresponds to $0°, 30°, 60°, 90°, 120°, 150°, 180°, 210°, 240°, 270°, 300°$ and $330°$ were used in this simulation as shown in figure 4.1.

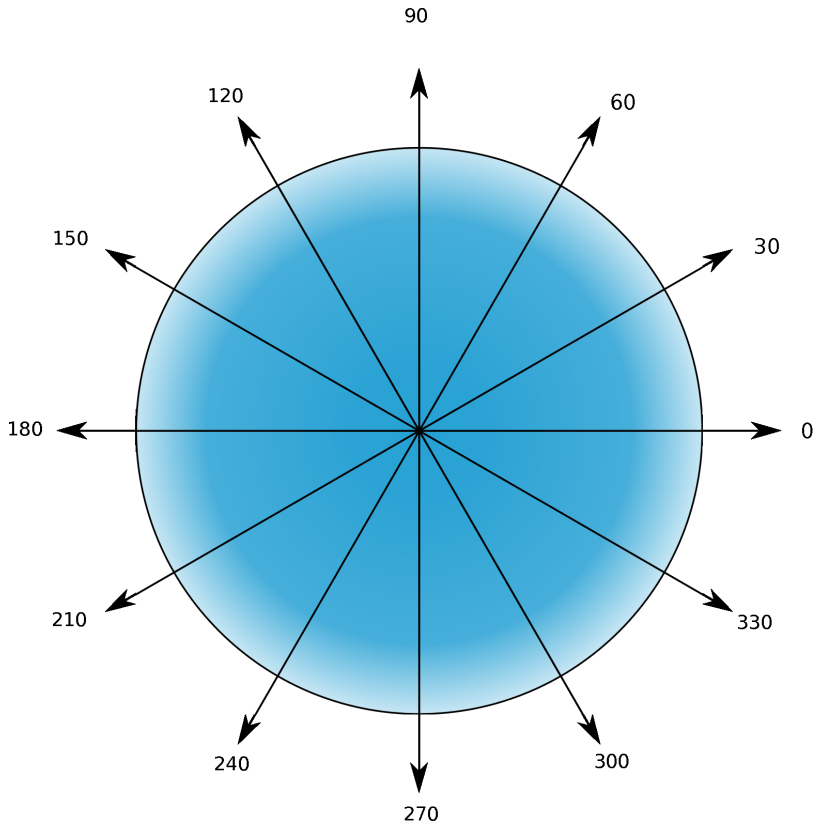

Figure 4.1: Different motion targets used in the simulation

The resulting cortical responses can be displayed as a movie showing colored map of the visual cortex changing with simulation time. Following figures shows selected set of fifteen frames from each simulation movie. The first simulation from each motion path was selected to generate movies.

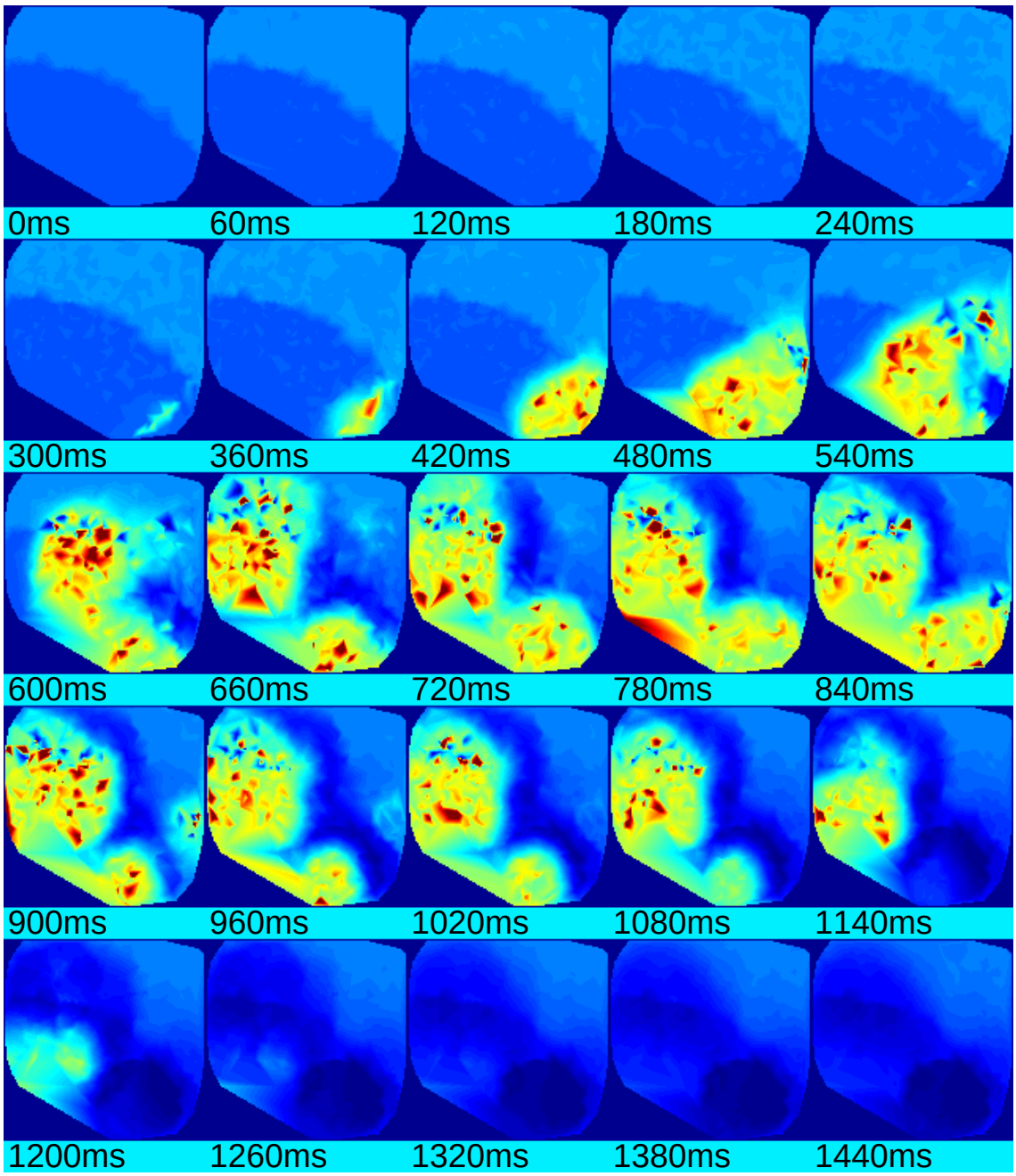

Figure 4.2: Cortical Response Movie frames for motion path corresponds to 0°

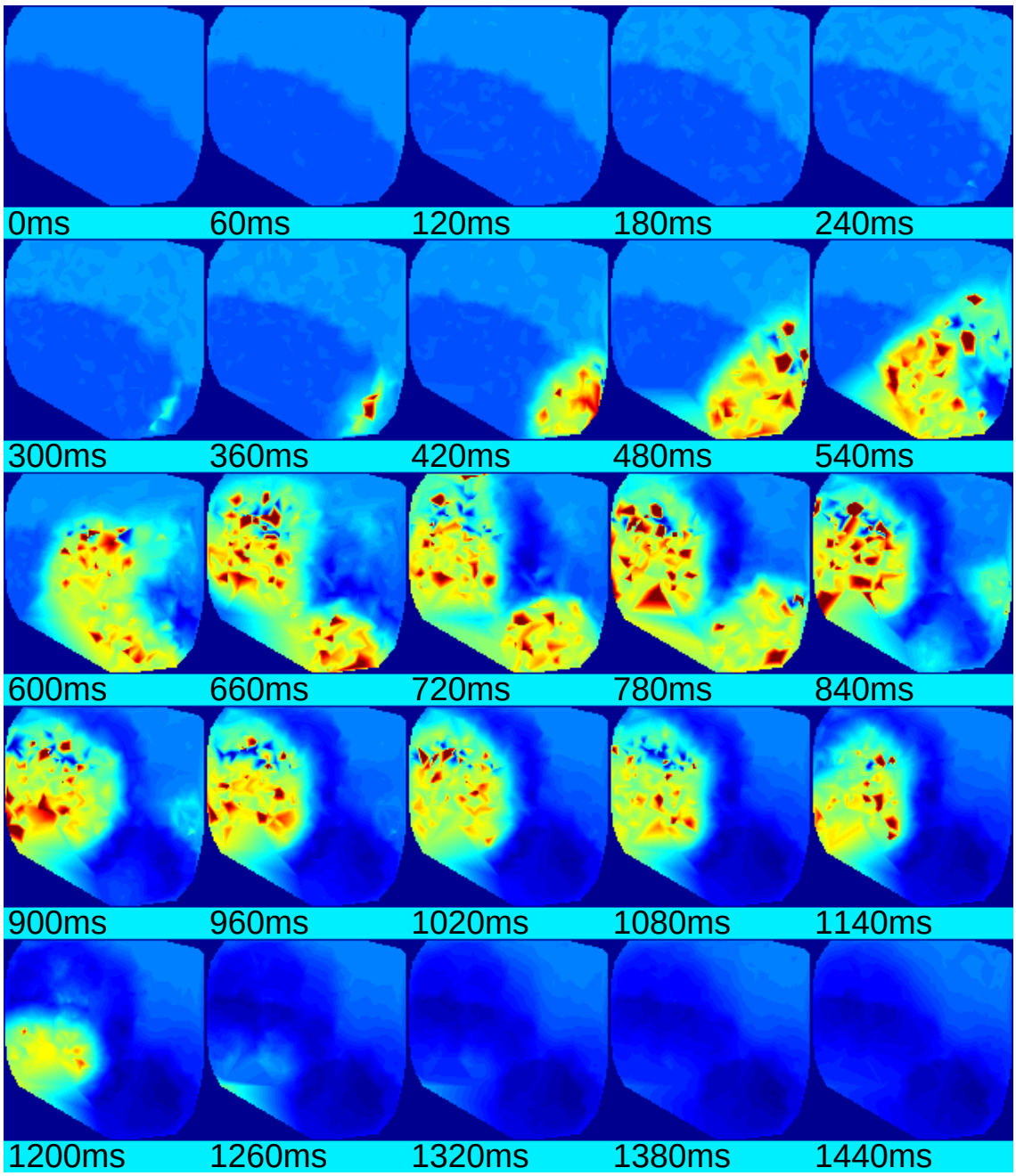

Figure 4.3: Cortical Response Movie frames for motion path corresponds to 30°

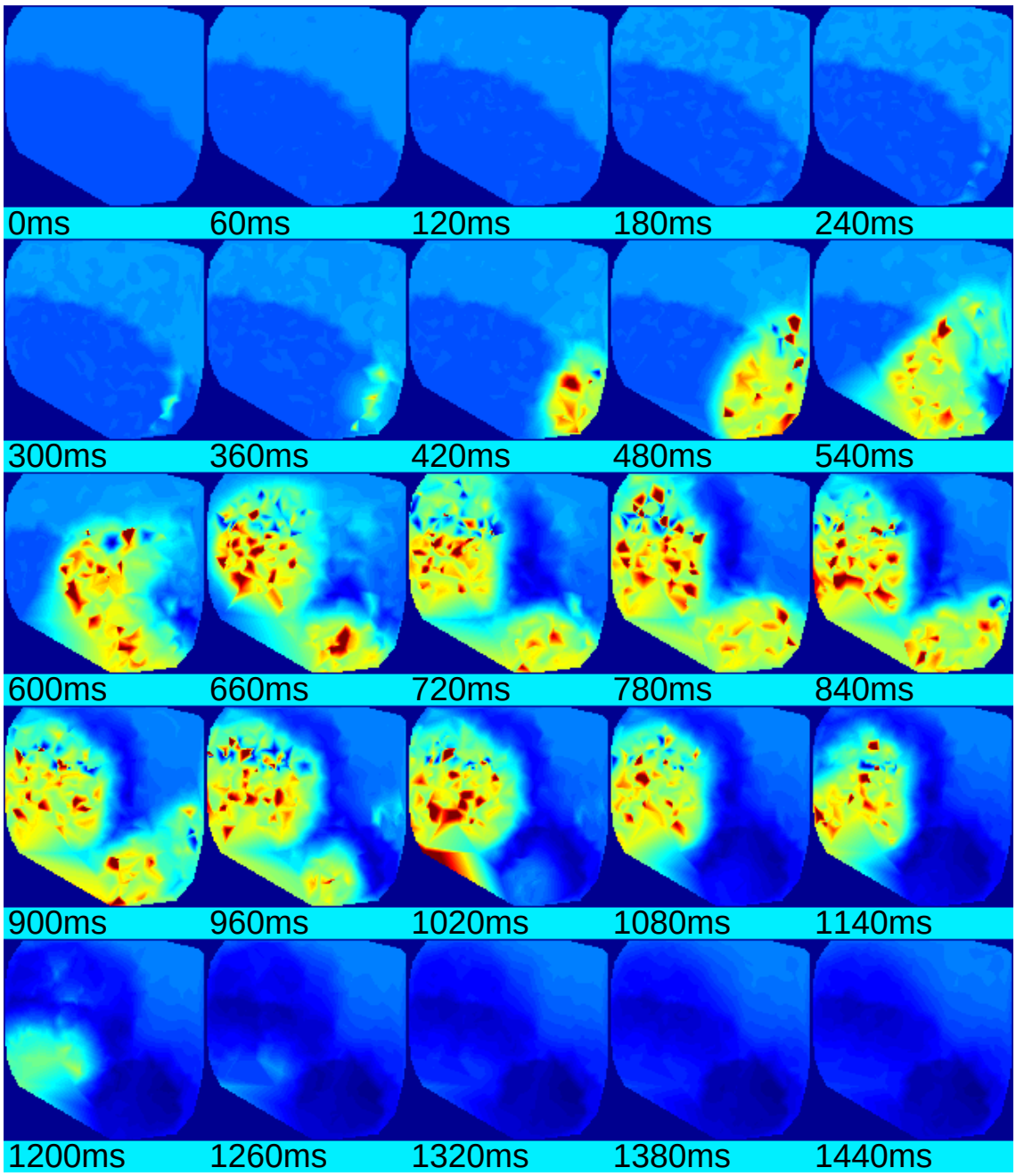

Figure 4.4: Cortical Response Movie frames for motion path corresponds to 60°

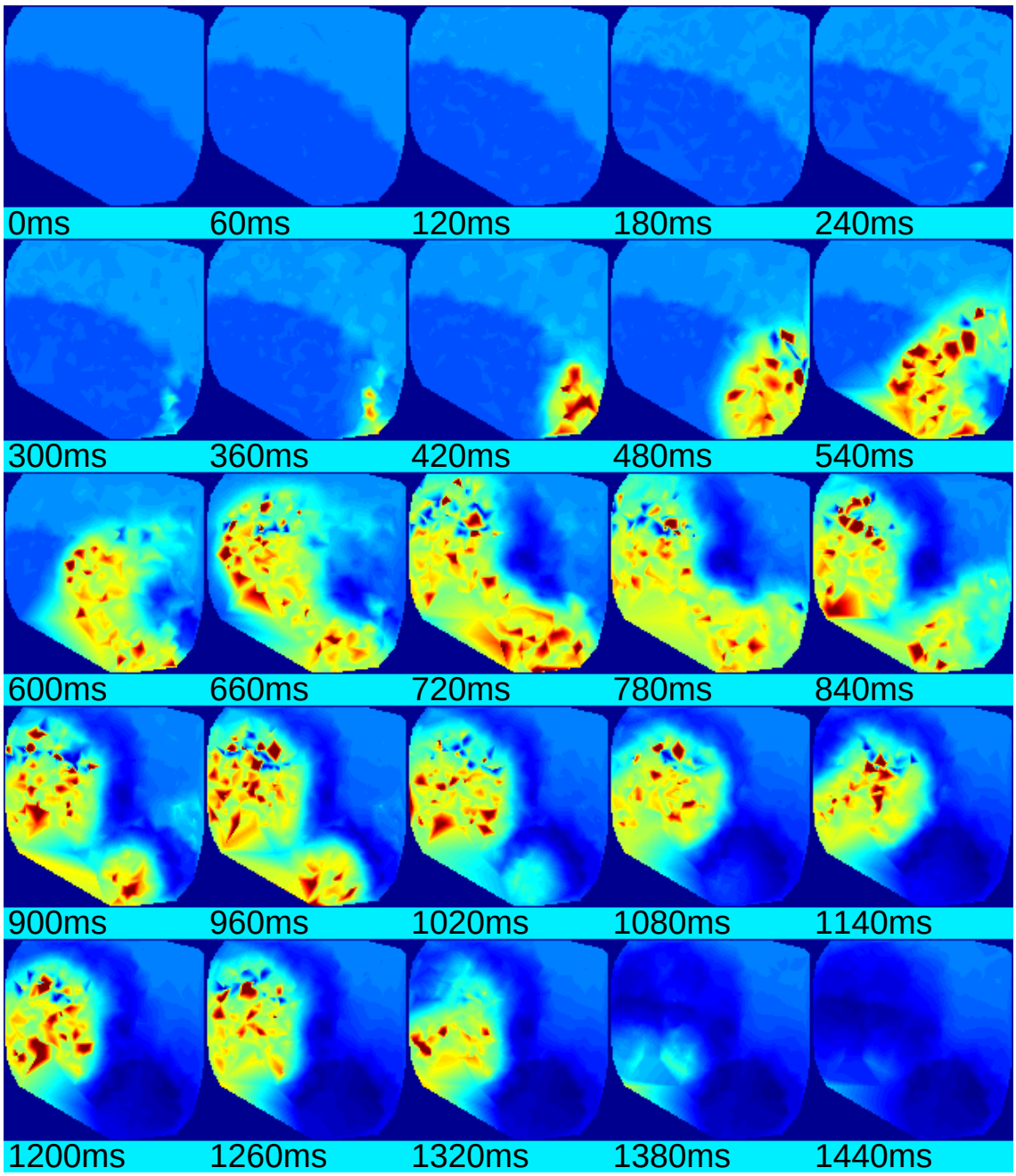

Figure 4.5: Cortical Response Movie frames for motion path corresponds to 90°

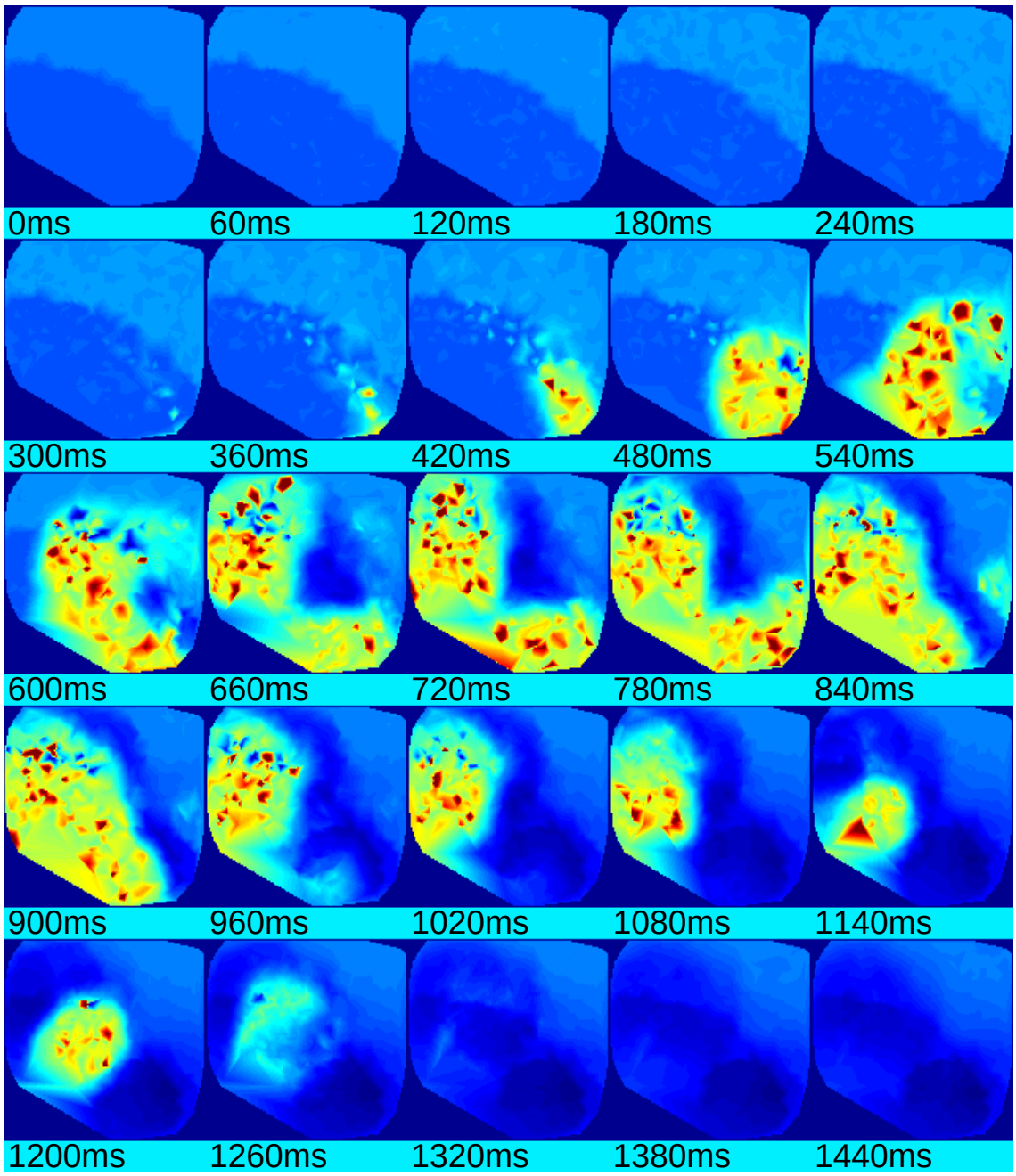

Figure 4.6: Cortical Response Movie frames for motion path corresponds to 120°

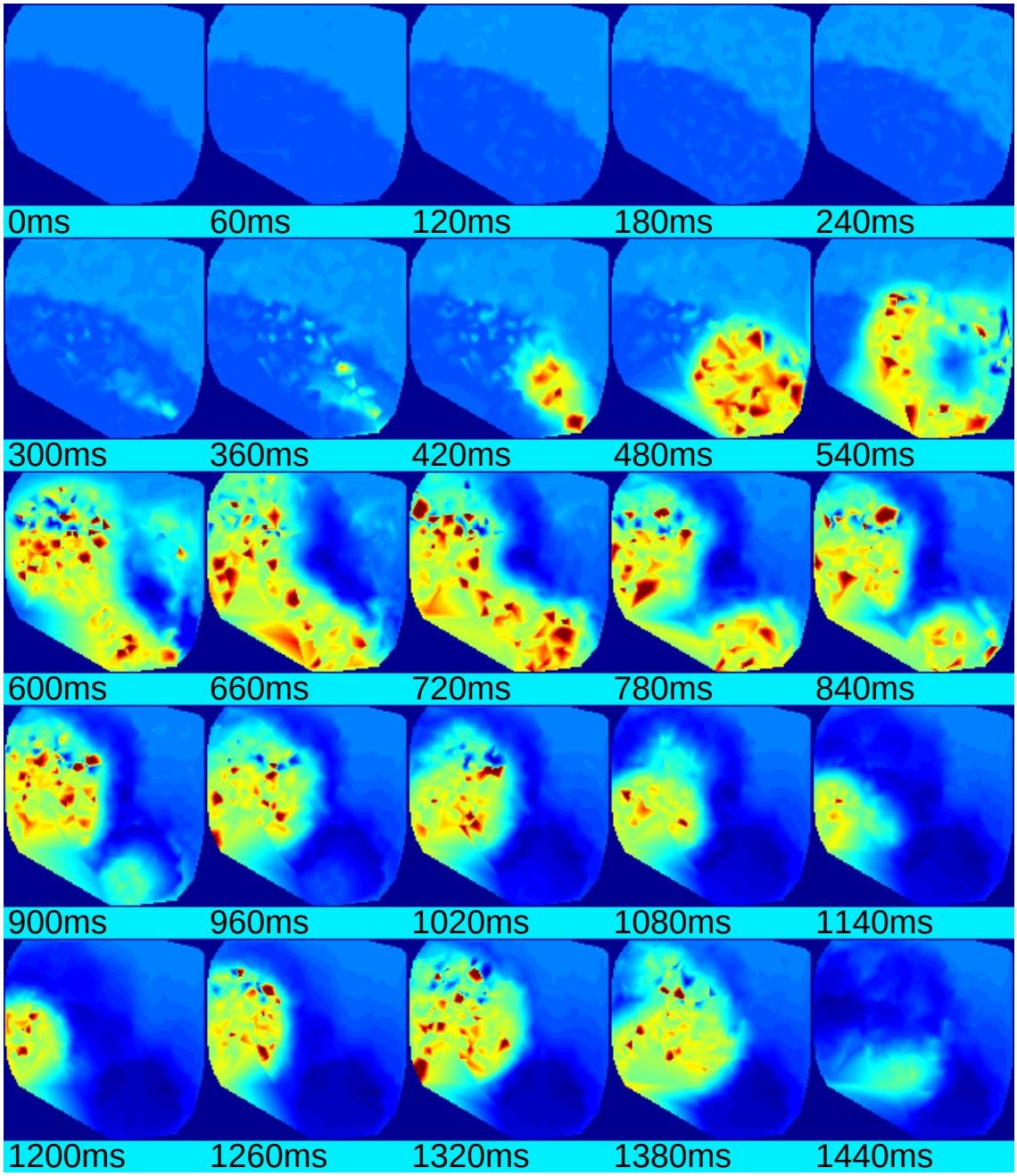

Figure 4.7: Cortical Response Movie frames for motion path corresponds to 150°

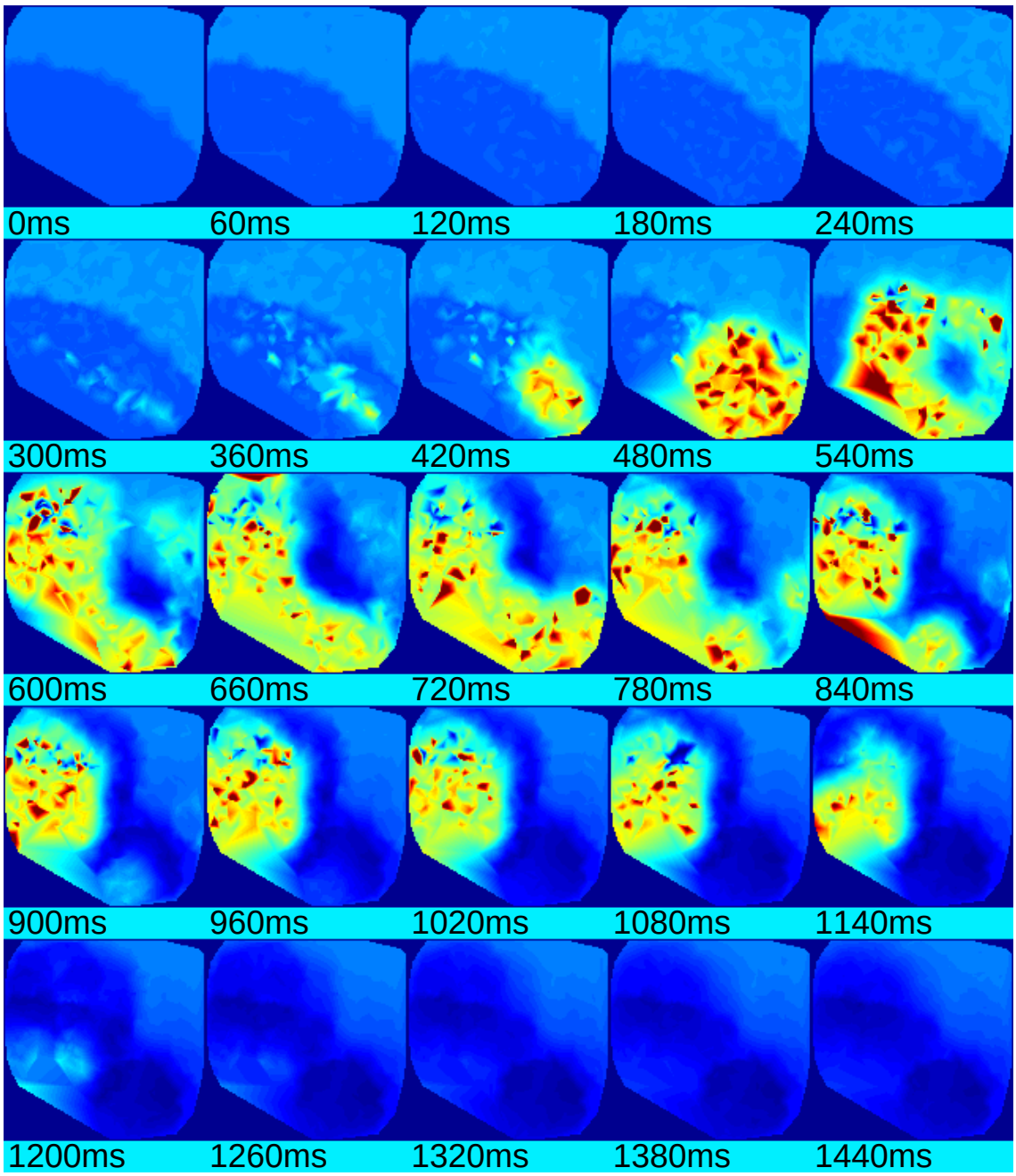

Figure 4.8: Cortical Response Movie frames for motion path corresponds to 180°

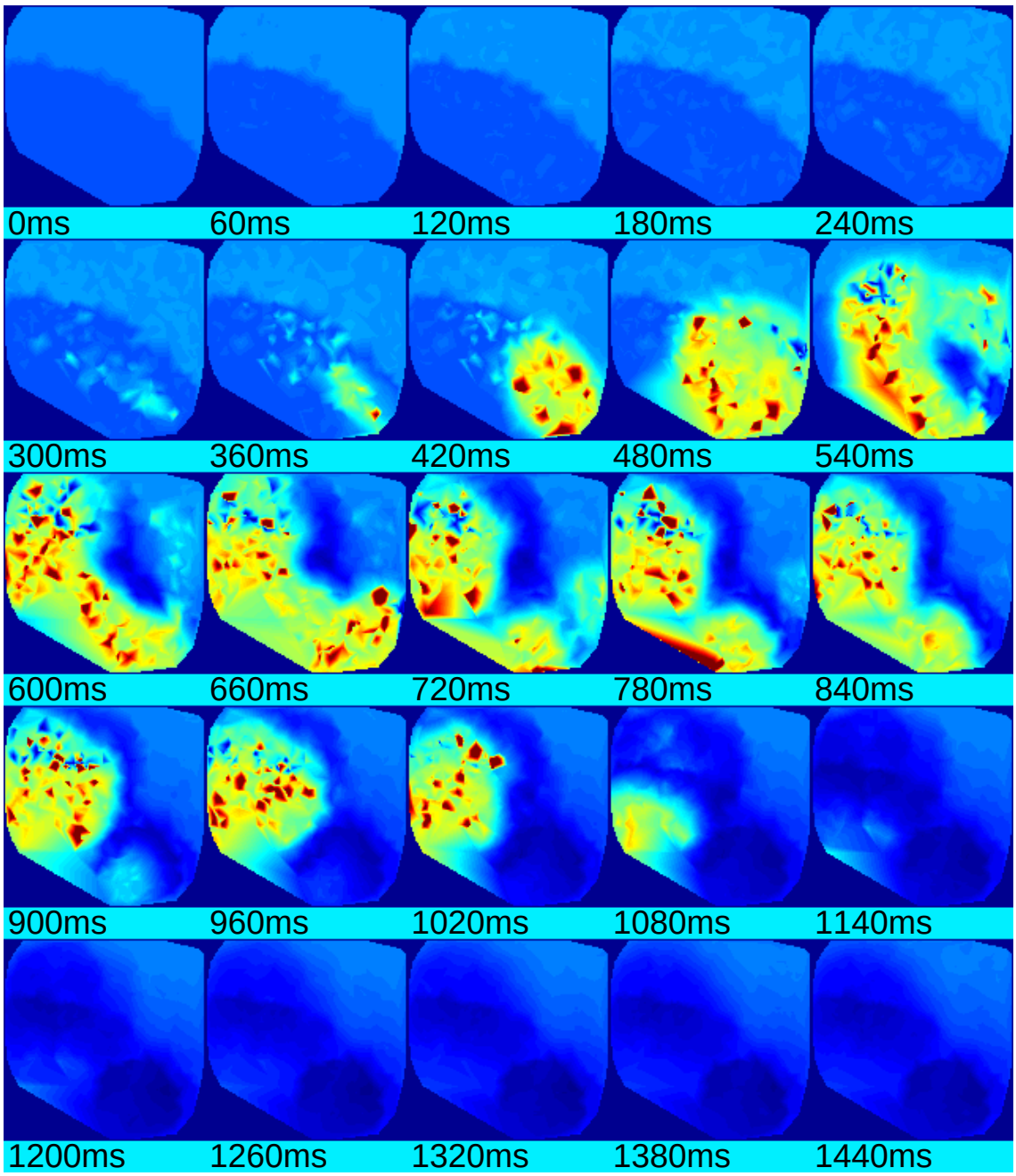

Figure 4.9: Cortical Response Movie frames for motion path corresponds to 210°

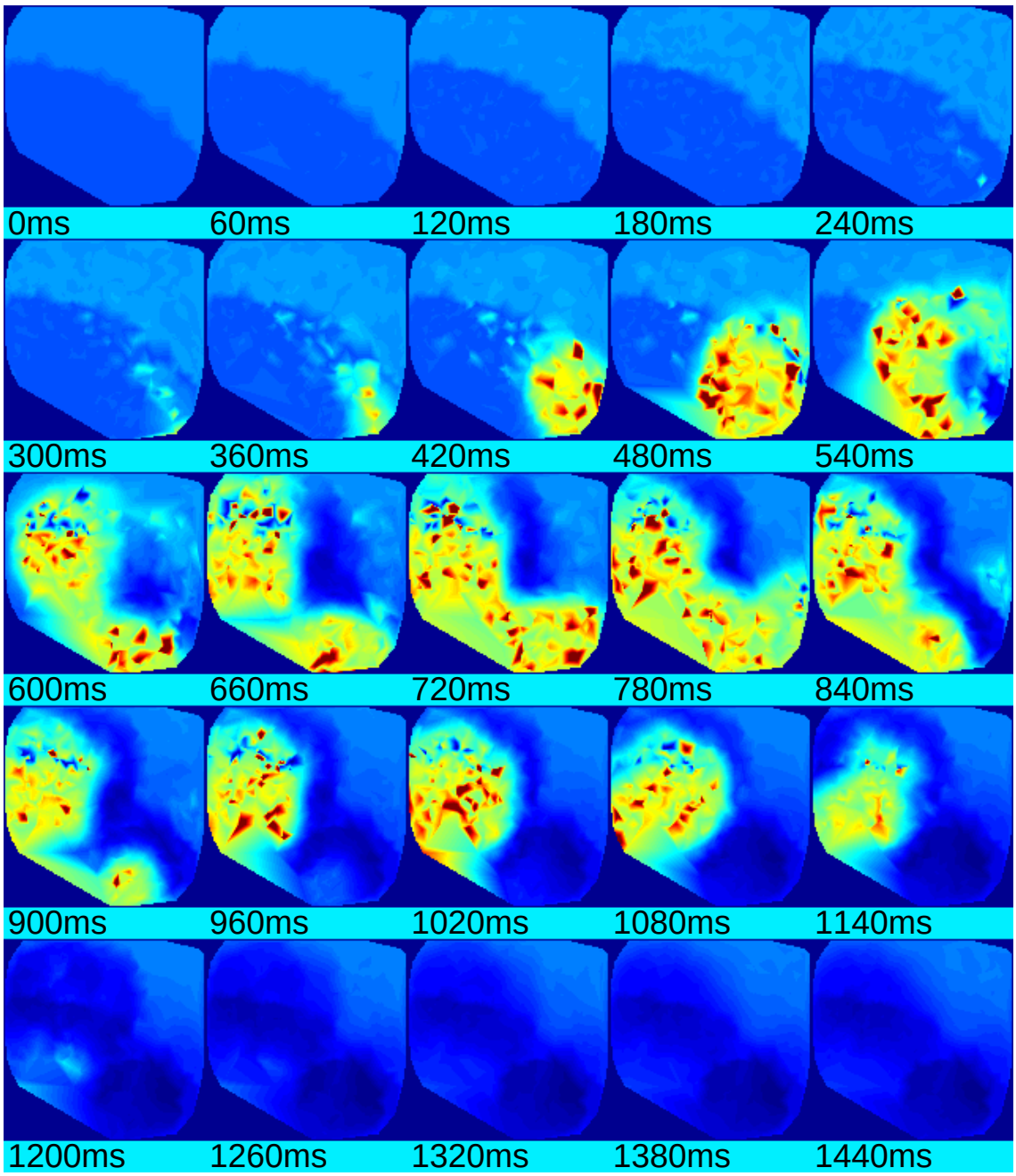

Figure 4.10: Cortical Response Movie frames for motion path corresponds to 240°

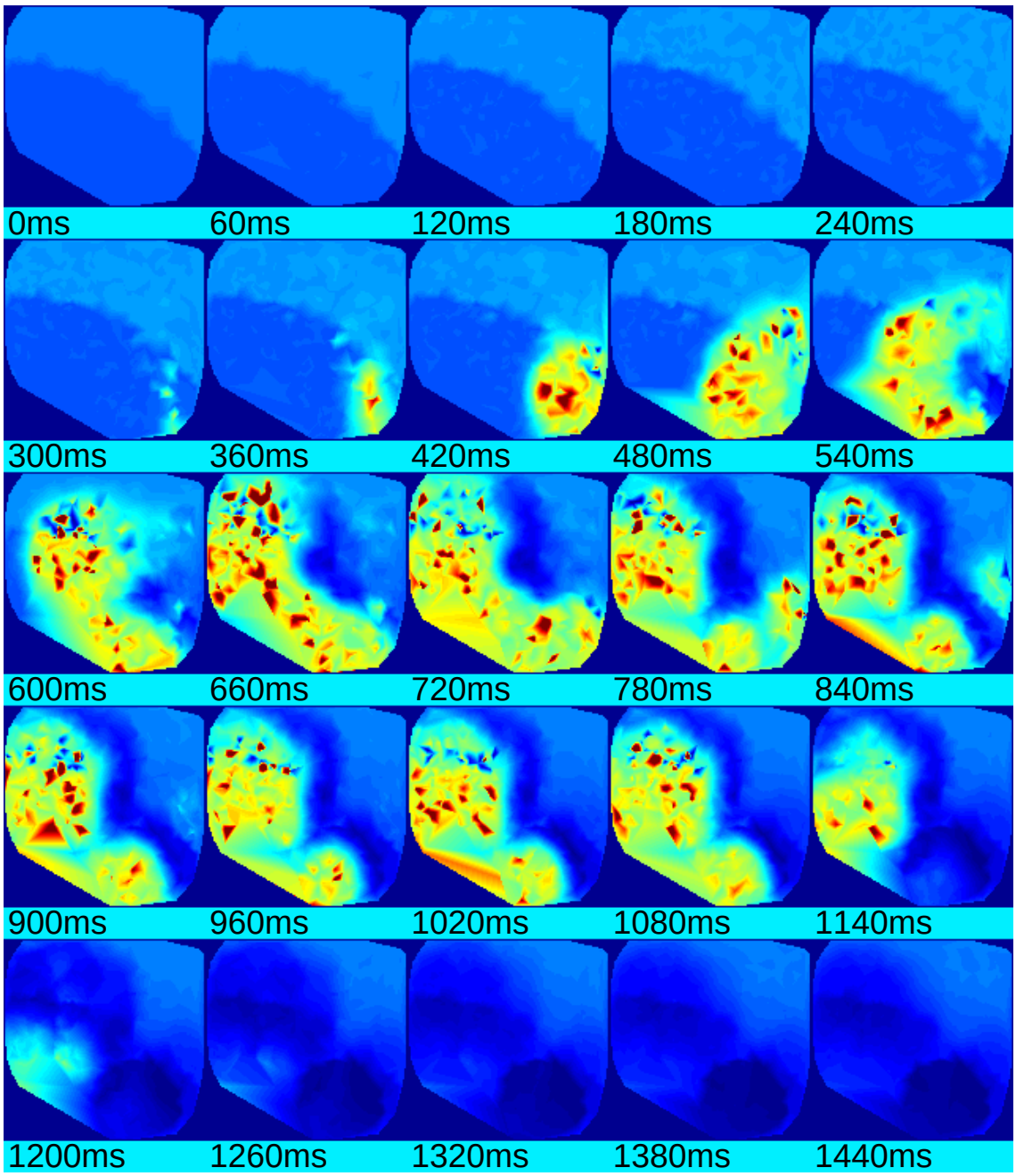

Figure 4.11: Cortical Response Movie frames for motion path corresponds to 270°

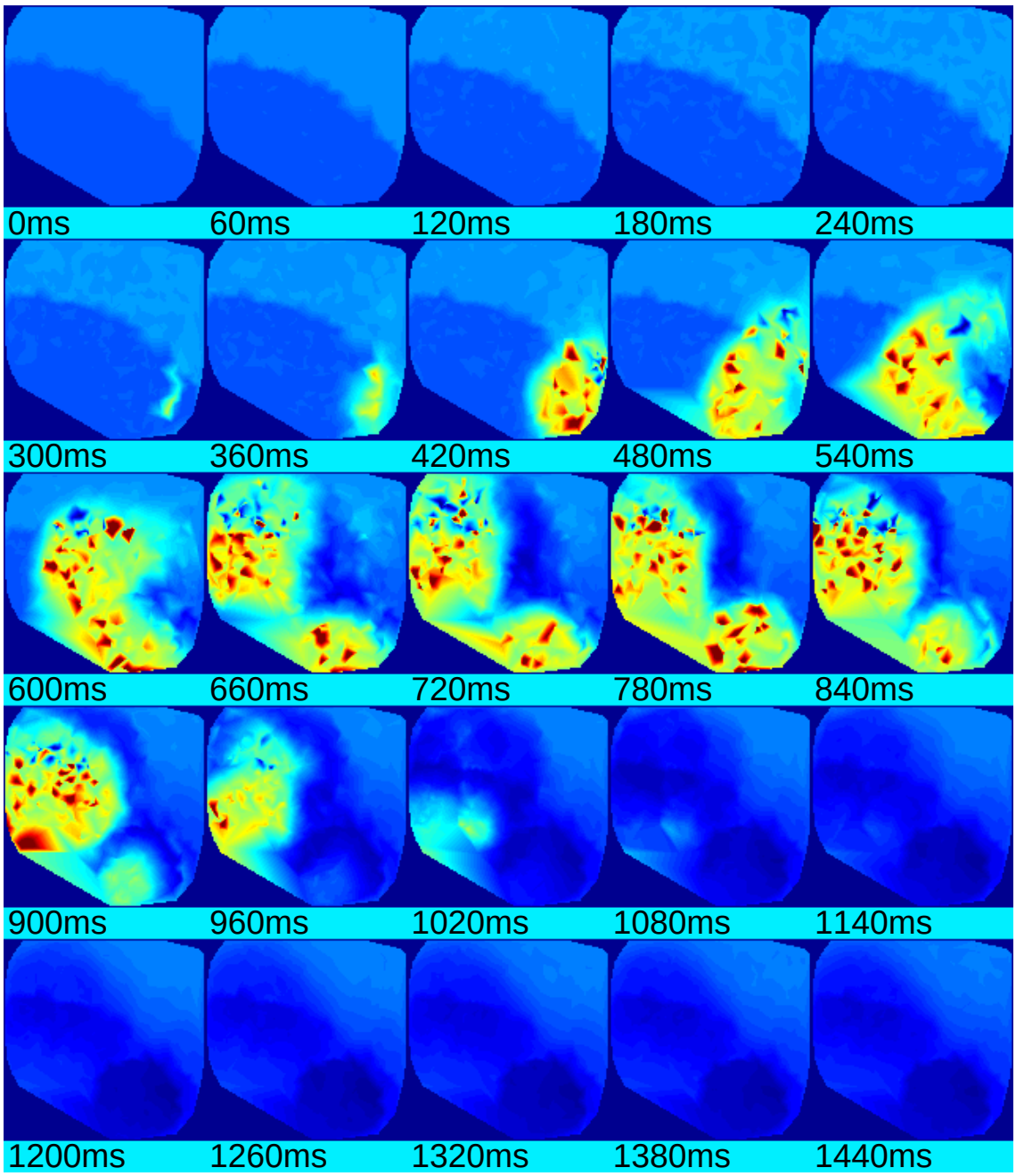

Figure 4.12: Cortical Response Movie frames for motion path corresponds to 300°

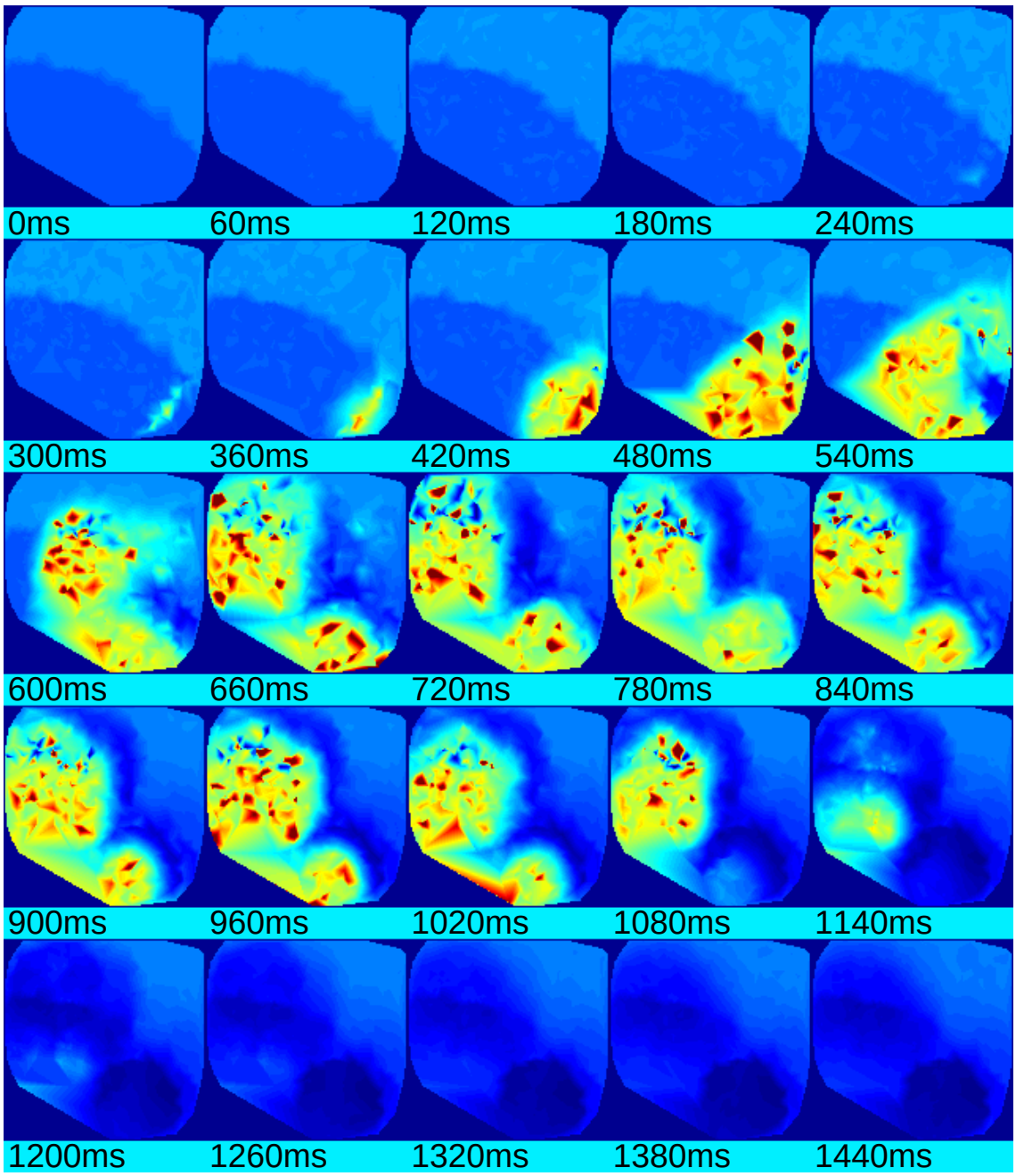

Figure 4.13: Cortical Response Movie frames for motion path corresponds to 330°

CHAPTER V
MOTION TARGET DISCRIMINATION

5.1 Low Pass Filtering

5.2 Two-Stage Principal Component Analysis

Principal component analysis is primarily used to reduce the dimensionality of the data while retaining as much information as encoded in the original data set. This is done by transforming the observed data into a new set of uncorrelated variables [6]. Even though the original Karhunen-Loeve transformation is used for continuous variables [6], we will be using a discretized variant of this original Karhunen-Loeve transformation [8], [3].

The response waves in the visual cortex can be considered as a movie consisting a sequence of frames, each showing the visual cortex activity level in points in the visual cortex. The information encoded in these waves can be encoded by a two-step Karhunen-Loeve (KL) decomposition as described on Nenadic *et al.* [8] and Du *et al.* [3]

In this analysis, a two-step KL-decomposition was used with a *sliding encoding window* was used to analyze the segments of cortical responses. As shown in figure 5.1, the time axis was covered by equal length, overlapping windows. The two-step KL-decomposition was applied to the segment of the spike rate signal within each window. The length of the sliding window remains constant while the starting and ending position of the window changes with time. As shown in [3], each segment of the cortical response is mapped to a point in the B-space.

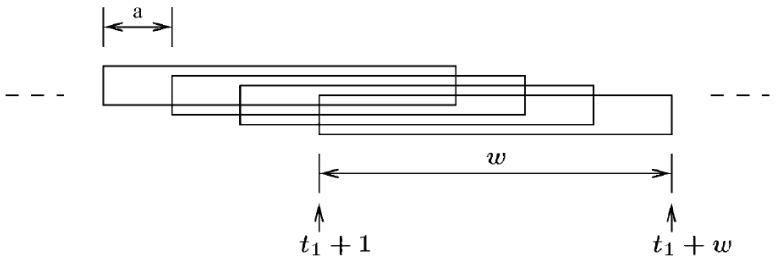

Figure 5.1: Sliding Encoding Window Technique

For a given motion target for the retina, let $I(t,n), 0 \leq t \leq T, 1 \leq n \leq N$ be the smoothed spike rate of the cell as a spatio-temporal response signal where t is the time and n is the index of the pyramidal neuron in the visual cortex.

$I(t,n)$ can be taken as a matrix whose t^{th} row represents the spike rate of each neuron at time t for the given motion target in the retina and each column represents the n^{th} pyramidal neuron in the visual cortex.

Let the length of each time window be w and let $I(t,n), t_1 + 1 \leq t \leq t_1 + w, t_1 = 0, a, 2a, ...$ be the response signals for different time windows. Here a is the amount of time that the encoding window slide (*See* figure 5.1).

Let M denote the the total number of cortical response movies in response to each motion target with motion angle $\theta = 0°, 30°, 60°, ..., 330°$. For the $k^{th}, k = 1, 2, ...M$ movie,the spatio-temporal signal in this time window can be considered as a collection of vectors $\{I^k(t_1+1), I^k(t_1+2), ..., I^k(t_1+w),\}$ where $I^k(t_1+i) \in \mathbb{R}^{1\times N}, i = 1, 2, ..., w$

The two-step KL-decomposition reduces the dimensionality of the cortical response into A-space and B-space respectively. First, let's consider the KL-transform into A-space.

The covariance matrix $C_1 \in \mathbb{R}^{N\times N}$ for M movies is calculated as,

$$C_1 = \frac{1}{Mw} \sum_{k=1}^{M} \sum_{i=1}^{w} (I^k(t_1 + i))^T (I^k(t_1 + i)) \tag{5.1}$$

where $(I^k(t_1 + i))^T$ is the transpose of $I^k(t_1 + i)$.

The matrix C_1 is symmetric and positive semi-definite and its eigenvalues are all real and non-negative. The corresponding eigenvectors forms an orthonormal basis in $\mathbb{R}^N$. The eigenvectors corresponds to the largest p eigenvalues of C_1 are called the principal eigenvectors or modes. The p^{th} order successive reconstruction of the spatio-temporal signal $I^k(t) \in \mathbb{R}^{1\times N}$ is given by

$$\hat{I^k}(t_1 + i) = \sum_{j=1}^{p} \alpha_j^k(t_1 + i)\phi_j^T, i = 1, 2, ..., w \tag{5.2}$$

where $\phi_j \in \mathbb{R}^{N\times 1}$ is the j^{th} principal eigenvector. The time coefficients $\alpha_j^k(t_1 + i)$ are given by $\alpha_j^k(t_1 + i) = \langle I^k(t_1 + i), \phi_j^T \rangle$

The coefficients $\alpha_j^k(t_1+i)$ of the KL-decomposition are uncorrelated in terms of j and we call $\alpha_j^k(t), t_1+1 \leq t \leq t_1+w, 1 \leq j \leq p$ the p^{th} order A-space representation of the movie segment within the corresponding time window for the k^{th} movie.

The vector function 5.3 can be viewed as a sample function of a vector random process [3].

$$[\alpha_1^k(t), \alpha_2^k(t), ..., \alpha_p^k(t)], t_1+1 \leq t \leq t_1+w \tag{5.3}$$

Now, let

$$\gamma_j^k = \begin{bmatrix} \alpha_j^k(t_1+1) \\ \alpha_j^k(t_1+2) \\ \vdots \\ \alpha_j^k(t_1+w) \end{bmatrix}, (\xi^k)^T = \begin{bmatrix} \gamma_1^k \\ \gamma_2^k \\ \vdots \\ \gamma_p^k \end{bmatrix}, \text{ where, } j = 1, 2, ..., p \tag{5.4}$$

Calculating the covariance matrix as in equation 5.1,

$$C_2 = \frac{1}{M} \sum_{k=1}^{M} (\xi^k)^T (\xi^k) \tag{5.5}$$

and the q^{th} order successive approximation of the k^{th} vector ξ^k is given by

$$\hat{\xi^k} = \sum_{j=1}^{q} \beta_j^k \psi_j^T \tag{5.6}$$

where $\psi_j, j = 1, 2, \cdots, q$ are the eigenvectors corresponding to the largest q eigenvalues of the matrix C_2. The coefficients β_j^k are found by orthogonal projection of ξ^k onto the j^{th} eigenvector $\beta_j^k = \langle \xi^k, \psi_j^T \rangle$.

The $\beta_j^k(t), t_1+1 \leq t \leq t_1+w, 1 \leq j \leq p$ is the p^{th} order B-space representation of the movie segment within the corresponding time window for the k^{th} movie.

Few β components capture the most information found in the original movie as per [3]. Therefore, in this simulation, only the first six β components were calculated. By repeating the above process for all sliding encoding windows for the total simulation time, a movie produces a β-strand as a vector-valued function of time.

5.3 Encoding with Mean β-strands

Figures 5.2a shows all β-strands calculated in this simulation. The figure 5.2b shows the mean β-strand of all twelve angles used in this simulation. The mean β-strand was calculated by calculating the statistical mean of of each β component for a given sliding encoding window over all repetitions of a given motion target.

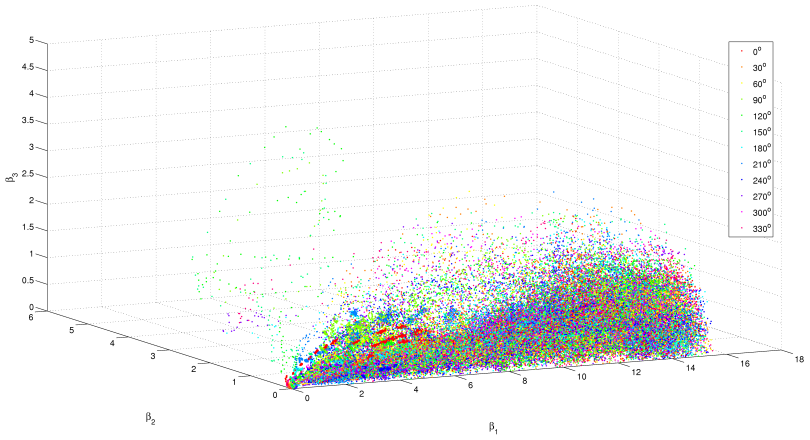

(a) β-strands for all motion targets

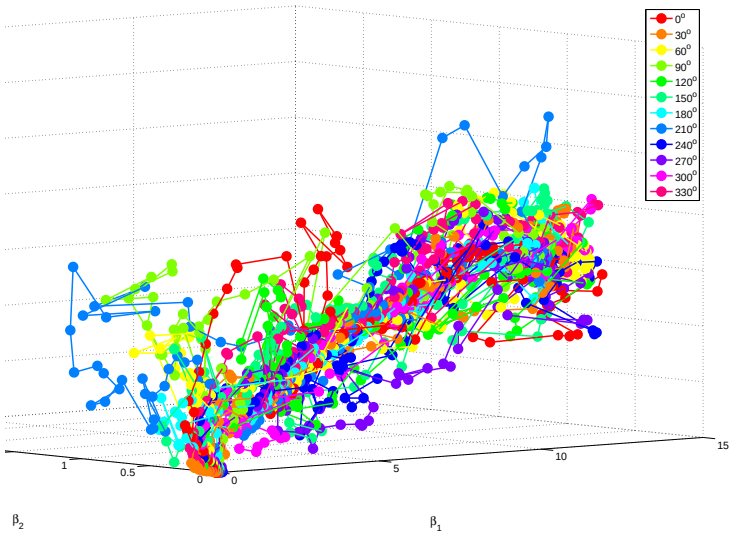

(b) Mean β-strands for all motion targets

Figure 5.2: β-strands and Mean β-strands for all motion targets, 0-1500ms

A more clear separation of β-strands can be seen in the figure 5.3 below and it shows the same β-strands and mean β-strands for sliding encoding windows up to 800ms of simulation time. Also, figures 5.4 - 5.15 shows β-strands and mean β-strands corresponds to three distinct motion targets per figure for sliding encoding windows up to 800ms of simulation time.

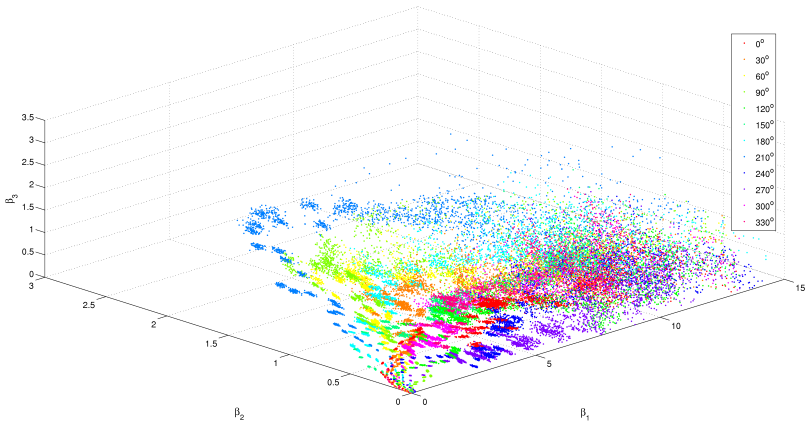

(a) β-strands for all motion targets

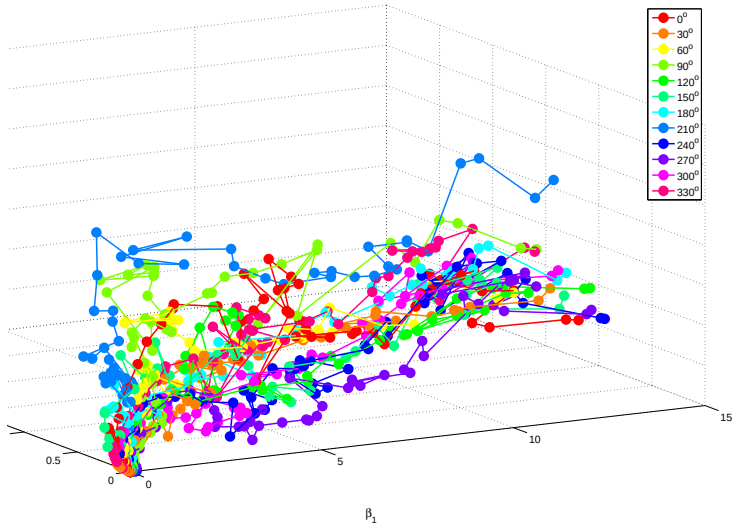

(b) Mean β-strands for all motion targets

Figure 5.3: β-strands and Mean β-strands for all motion targets, 0-800ms

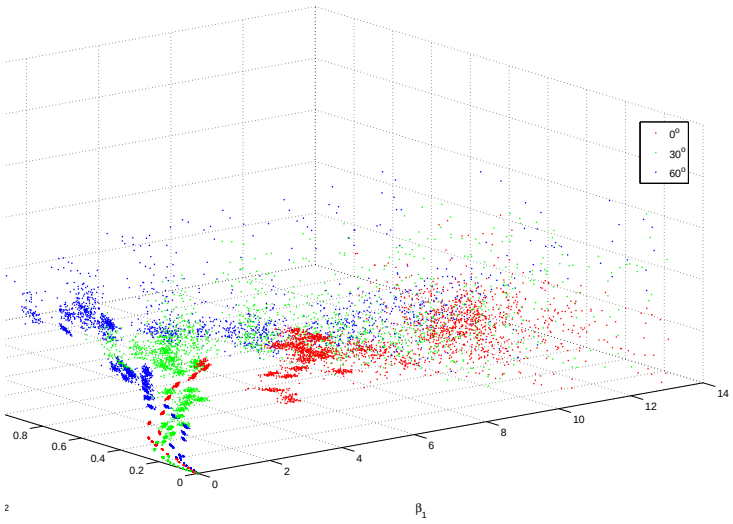

(a) β-strands for motion targets $0°, 30°$ and $60°$

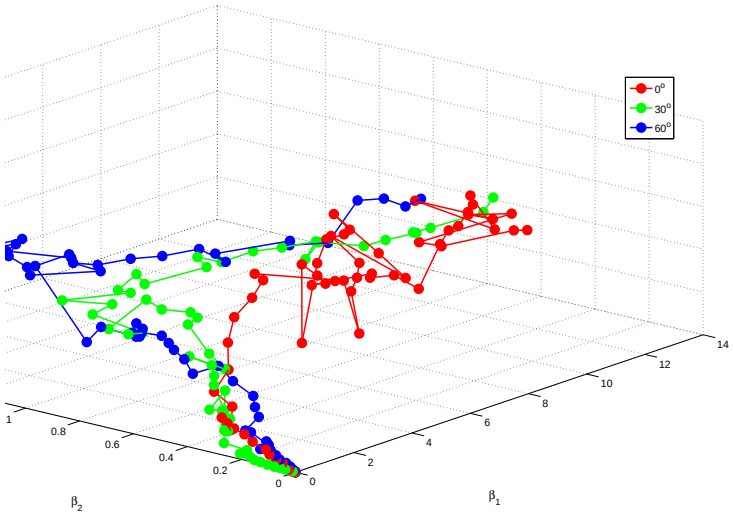

(b) Mean β-strands for motion targets $0°, 30°$ and $60°$

Figure 5.4: β-strands and Mean β-strands for motion targets $0°, 30°$ and $60°$, 0-800ms

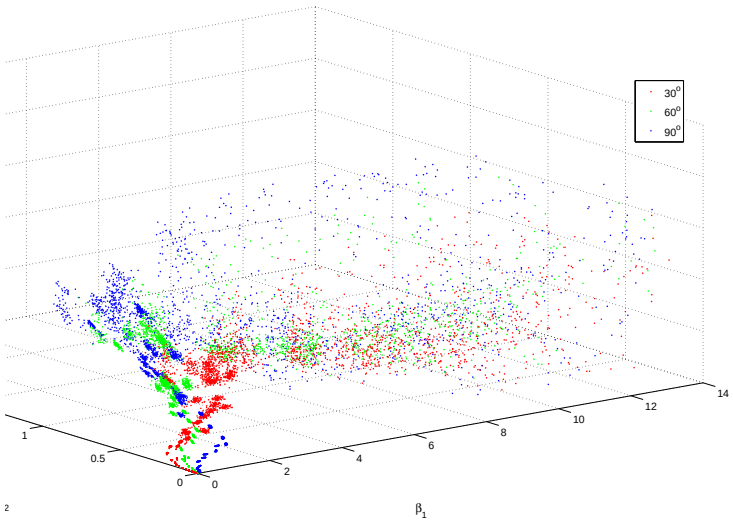

(a) β-strands for motion targets $30°, 60°$ and $90°$

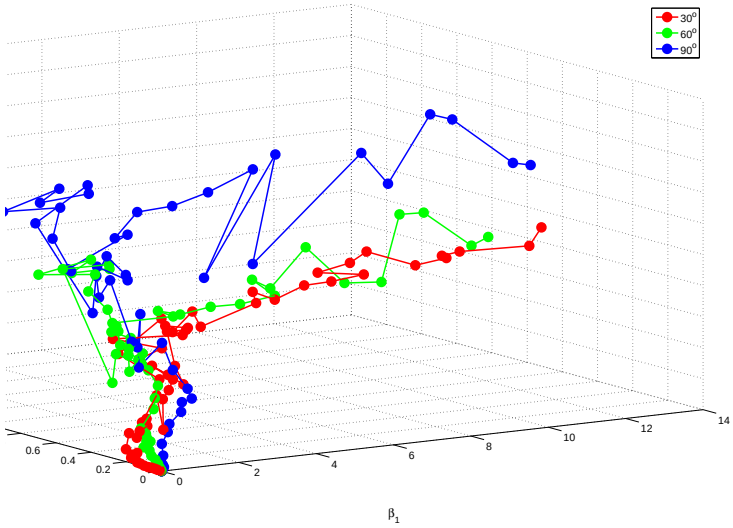

(b) Mean β-strands for motion targets $30°, 60°$ and $90°$

Figure 5.5: β-strands and Mean β-strands for motion targets $30°, 60°$ and $90°$, 0-800ms

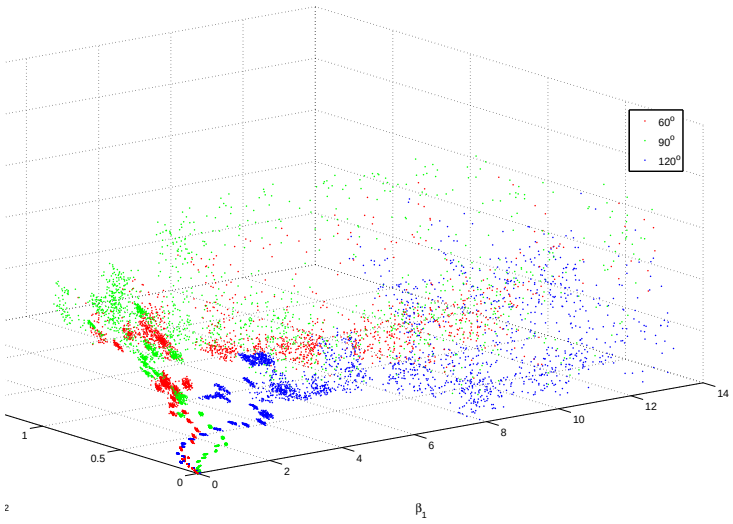

(a) β-strands for motion targets $60°, 90°$ and $120°$

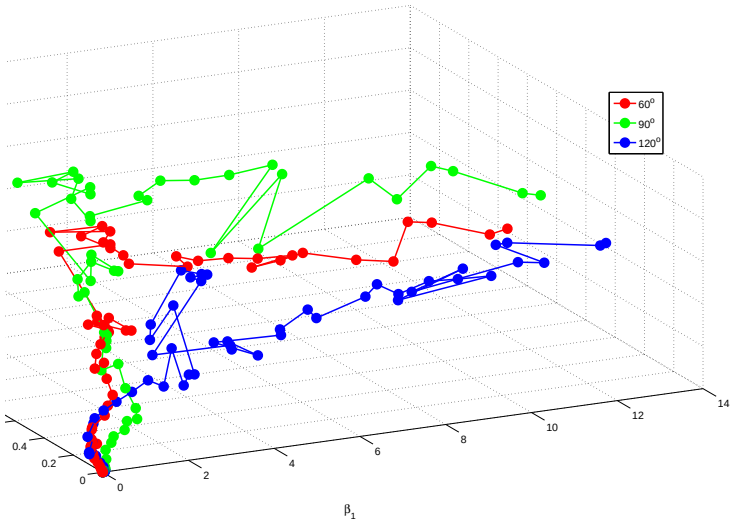

(b) Mean β-strands for motion targets $60°, 90°$ and $120°$

Figure 5.6: β-strands and Mean β-strands for motion targets $60°, 90°$ and $120°$, 0-800ms

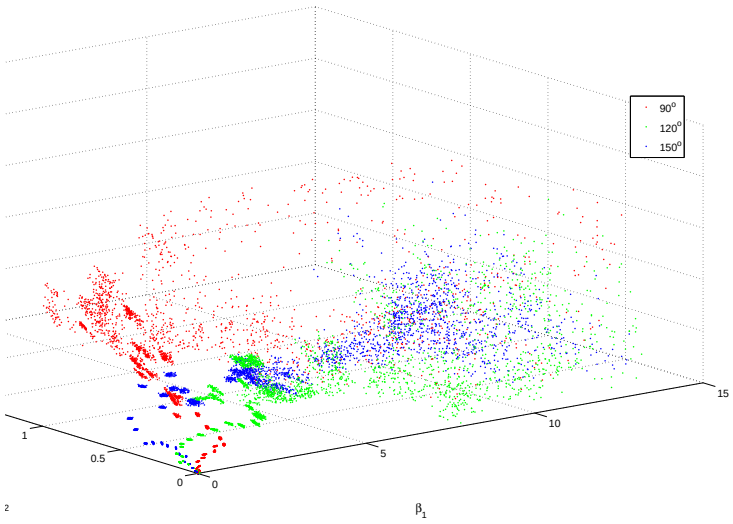

(a) β-strands for motion targets $90°, 120°$ and $150°$

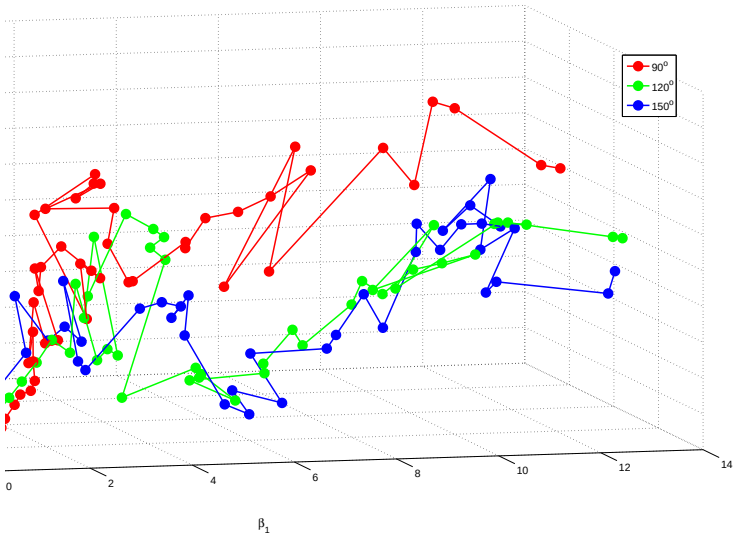

(b) Mean β-strands for motion targets $90°, 120°$ and $150°$

Figure 5.7: β-strands and Mean β-strands for motion targets $90°, 120°$ and $150°$, 0-800ms

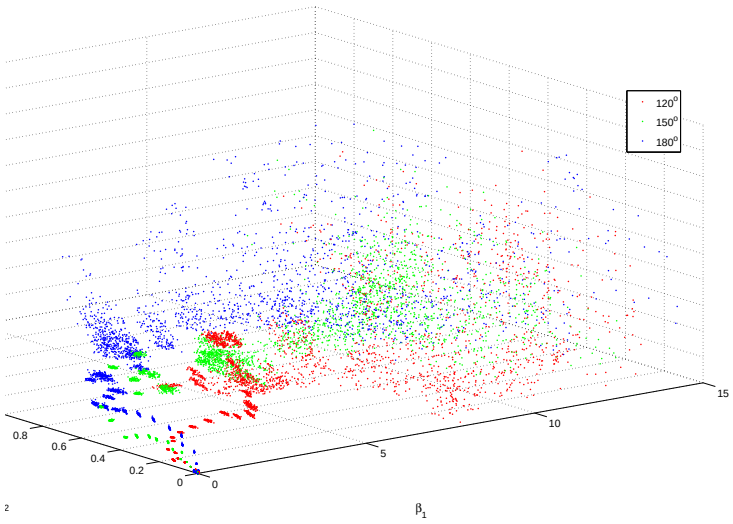

(a) β-strands for motion targets $120°, 150°$ and $180°$

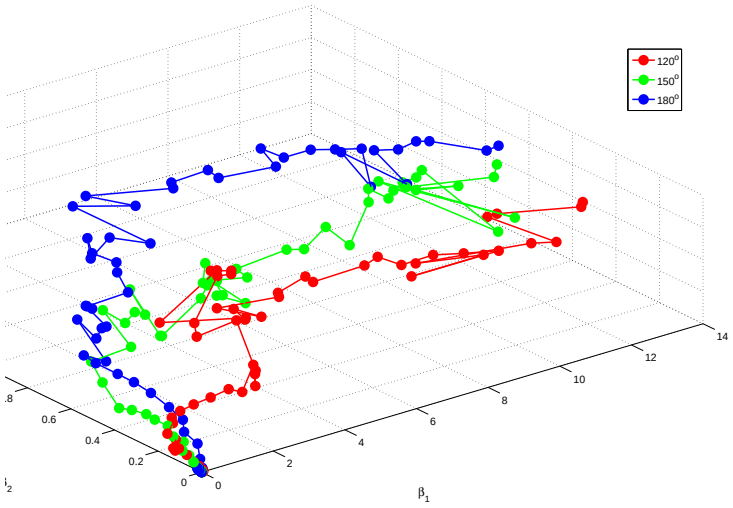

(b) Mean β-strands for motion targets $120°, 150°$ and $180°$

Figure 5.8: β-strands and Mean β-strands for motion targets $120°, 150°$ and $180°$, 0-800ms

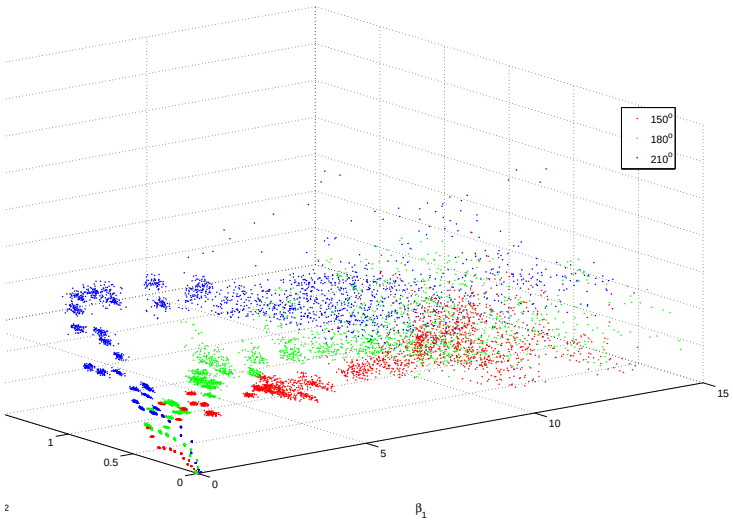

(a) β-strands for motion targets $150°, 180°$ and $210°$

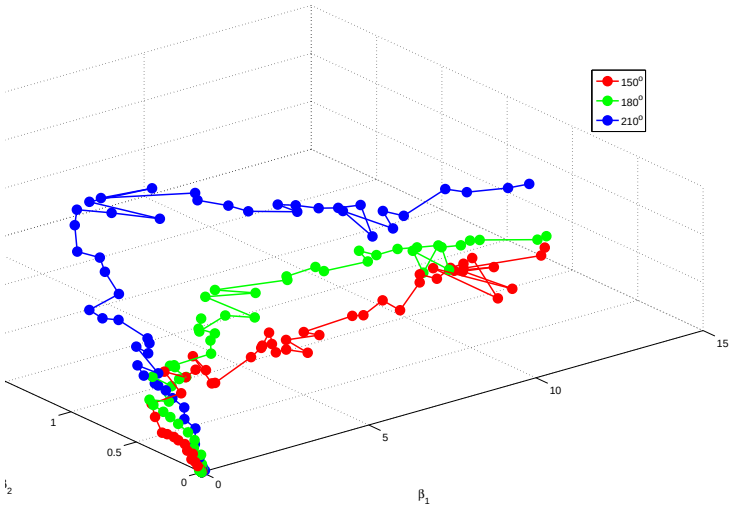

(b) Mean β-strands for motion targets $150°, 180°$ and $210°$

Figure 5.9: β-strands and Mean β-strands for motion targets $150°, 180°$ and $210°$, 0-800ms

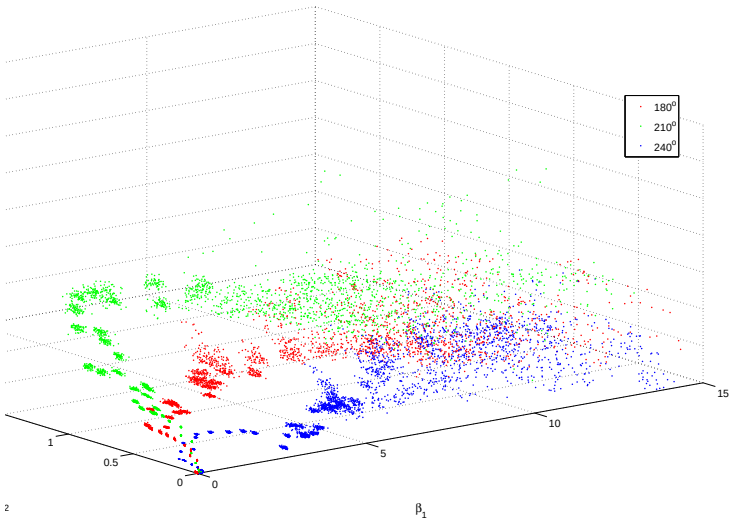

(a) β-strands for motion targets $180°, 210°$ and $240°$

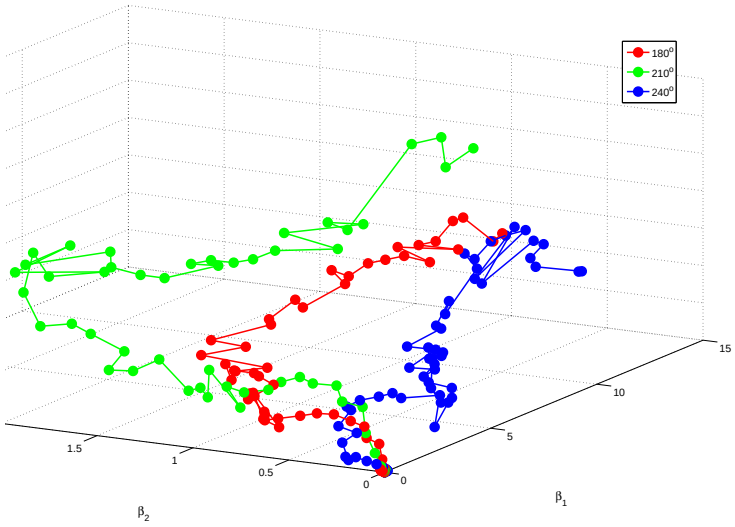

(b) Mean β-strands for motion targets $180°, 210°$ and $240°$

Figure 5.10: β-strands and Mean β-strands for motion targets $180°, 210°$ and $240°$, 0-800ms

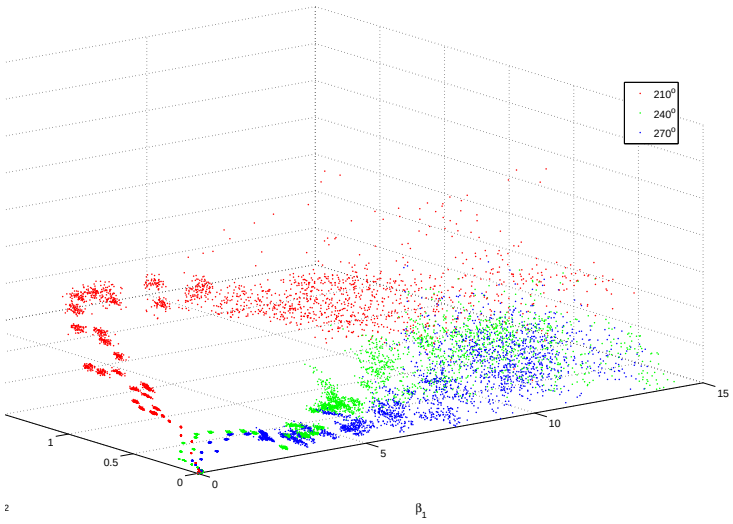

(a) β-strands for motion targets $210°, 240°$ and $270°$

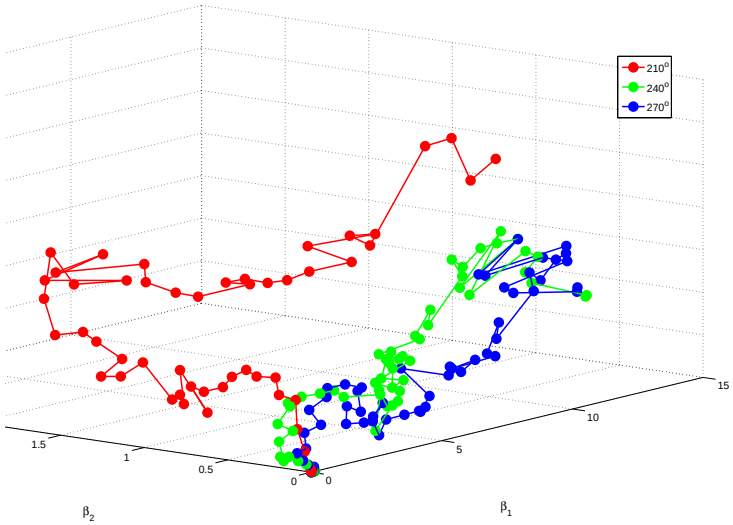

(b) Mean β-strands for motion targets $210°, 240°$ and $270°$

Figure 5.11: β-strands and Mean β-strands for motion targets $210°, 240°$ and $270°$, 0-800ms

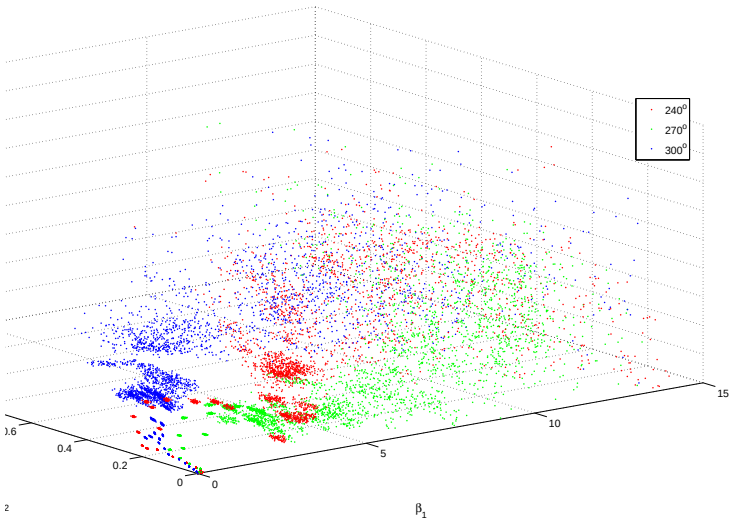

(a) β-strands for motion targets $240°, 270°$ and $300°$

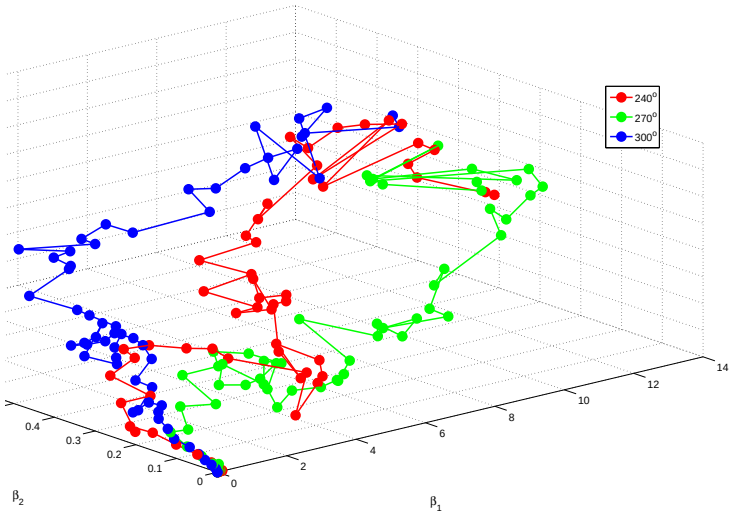

(b) Mean β-strands for motion targets $240°, 270°$ and $300°$

Figure 5.12: β-strands and Mean β-strands for motion targets $240°, 270°$ and $300°$, 0-800ms

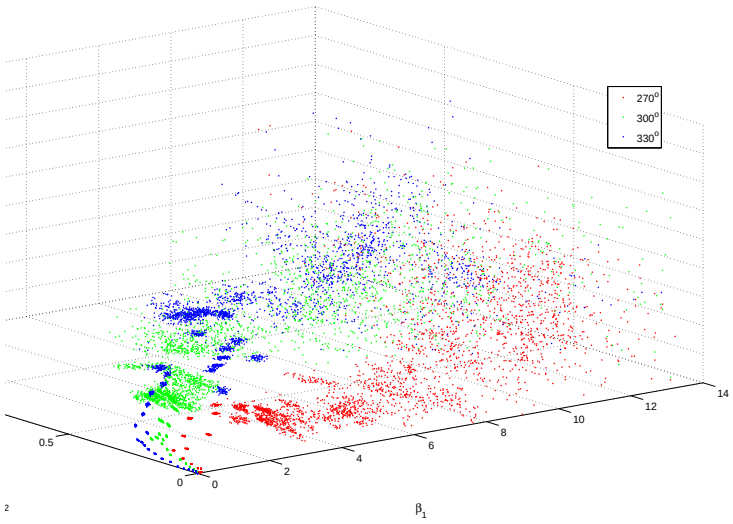

(a) β-strands for motion targets $270°, 300°$ and $330°$

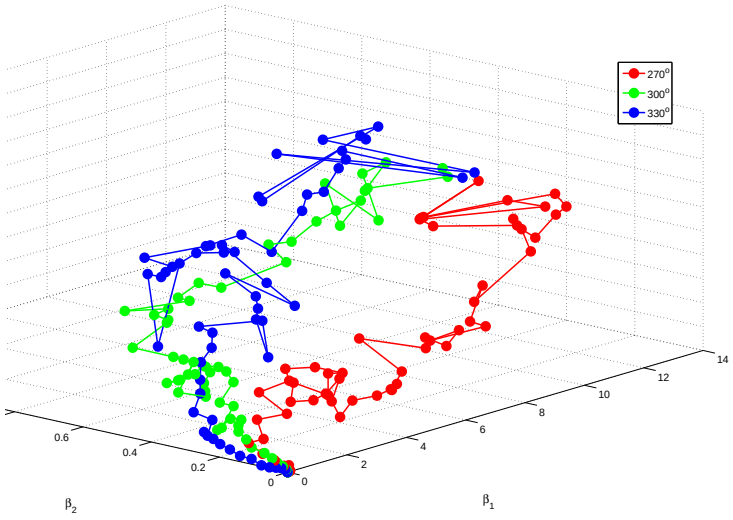

(b) Mean β-strands for motion targets $270°, 300°$ and $330°$

Figure 5.13: β-strands and Mean β-strands for motion targets $270°, 300°$ and $330°$, 0-800ms

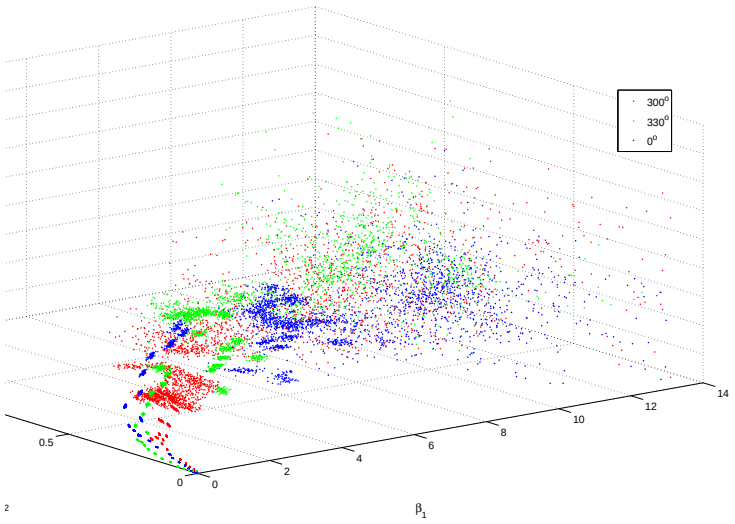

(a) β-strands for motion targets $300°, 330°$ and $0°$

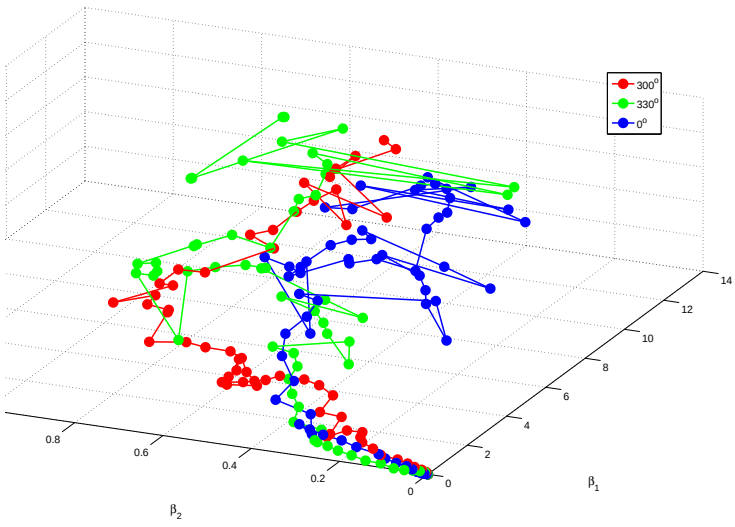

(b) Mean β-strands for motion targets $300°, 330°$ and $0°$

Figure 5.14: β-strands and Mean β-strands for motion targets $300°, 330°$ and $0°$, 0-800ms

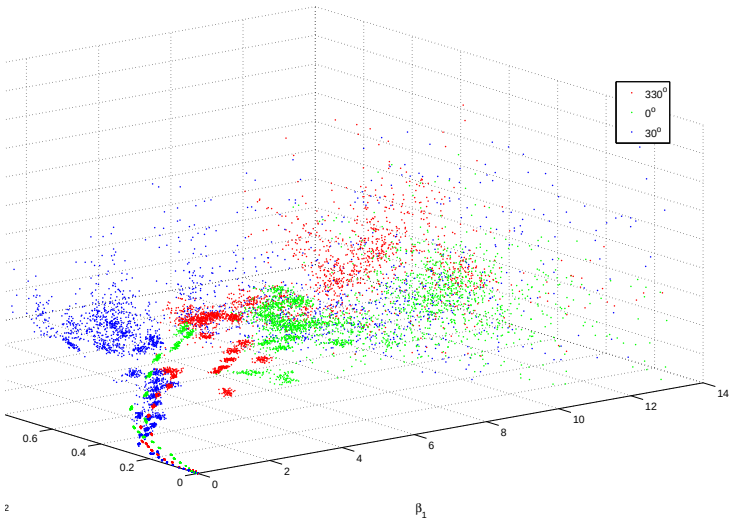

(a) β-strands for motion targets $330°, 0°$ and $30°$

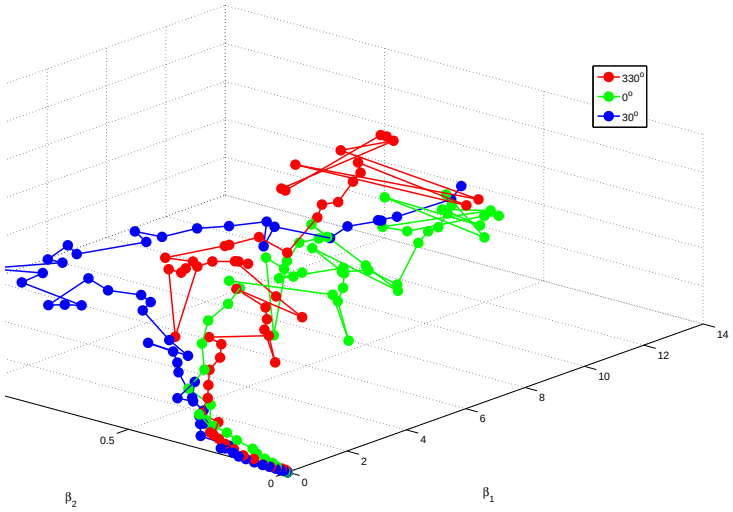

(b) Mean β-strands for motion targets $330°, 0°$ and $30°$

Figure 5.15: β-strands and Mean β-strands for motion targets $330°, 0°$ and $30°$, 0-800ms

The mean β-strands for each input stimuli corresponds to each motion target is denoted by $s_{0°}(t), s_{30°}(t), s_{60°}(t), \cdots, s_{330°}(t)$ respectively. Let $r(t)$ denote the β-

strand of an arbitrary cortical movie in response to a input stimulus from an unknown motion path. We can denote the start and end times of a detection window as T_1 and T_2 respectively. Then, $T = T_2 - T_1$ gives the size of our detection window. The distance between two β-strands can be calculated as

$$d_{\theta_1\theta_2} = \sum_{t=T_1}^{T_2} \sum_{k=1}^{q} \left(s_{\theta_1}^k(t) - s_{\theta_2}^k(t)\right)^2, \theta_1, \theta_2 = 0^\circ, 30^\circ, 60^\circ, \cdots, 330^\circ \tag{5.7}$$

where k is the index of the component of $s_\theta(t), \theta = 0^\circ, 30^\circ, 60^\circ, \cdots, 330^\circ$.

The figure 5.16a shows this distance for all possible input stimuli for the entire simulation time. Figure 5.16b shows the same distance up to ending time $T_2 = 800ms$. All these distances can be seen reaching their maximum in the interval 400ms - 700ms. Most of these distances reach their maximum at 490ms and 650ms. Even though the distance seems increasing again after 1000ms, a clear pattern cannot be seen. Therefore, figure 5.16b shows that the detection is more accurate around 490ms and 560ms.

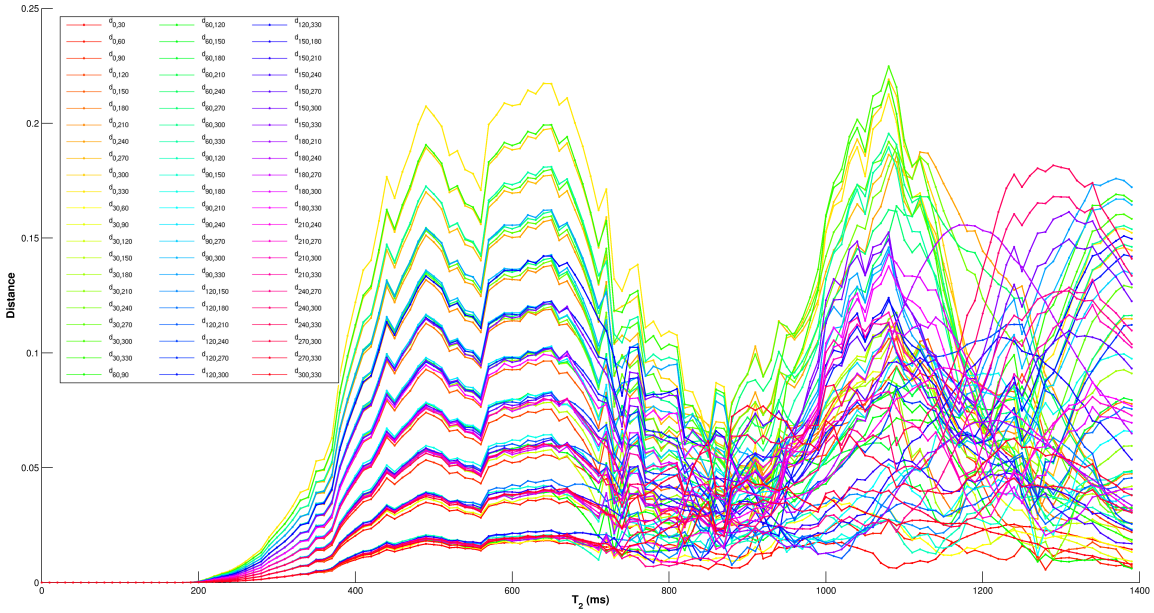

(a) For all ending times

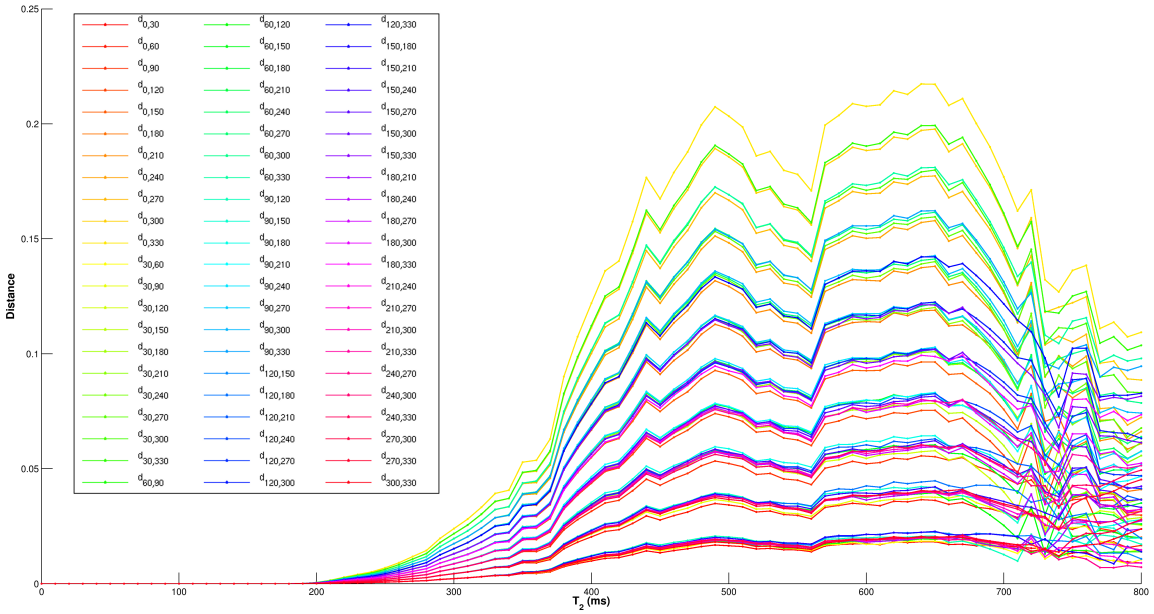

(b) For ending time $\leq$ 800ms

Figure 5.16: Distance between mean β-strands vs ending time T_2

5.4 Hypothesis Testing

With the white noise present in the simulation of the visual cortex model, a hypothesis testing problem can be formulated as discussed in [3]. We can extend and generalize our discussion of hypothesis testing from three inputs shown in [3] to twelve inputs corresponds to twelve motion paths used in this simulation and further in to any number of input stimuli.

Let the twelve input stimuli corresponds to each motion path angle associate with twelve hypotheses. $H_\theta, \theta = 0°, 30°, 60°, \cdots, 330°$ where H_θ denotes the hypothesis that the stimulus is from the motion target corresponds to motion angle $\theta°$. Therefore, we can write

$$r(t) = s_\theta(t) + n(t), \theta = 0°, 30°, 60°, \cdots, 330° \tag{5.8}$$

where $n(t)$ is the vector values noise process contained in the β-strand with mean 0.

The hypothesis testing used in this simulation was based on calculating conditional probability densities and selecting a decision criterion (See [3] and [20]). Here we use the Neyman-Pearson criteria as the decision criteria. Hypotheses are governed by probability assignments $P_j, j = 1, 2, 3, ...$ where hypothesis H_{θ_1} occurs with probability P_1, hypothesis H_{θ_2} occurs with probability P_2, hypothesis H_{θ_3} occurs with probability P_3, and so on.

By assigning the cost of correct detection to be zero and the cost of wrong detection to be one, from [20] the logarithm likelihood ratio is calculated as,

$$\ln \Lambda_1 (r(t)) = \frac{p_{r|H_{\theta_2}}(R|H_{\theta_2})}{p_{r|H_{\theta_1}}(R|H_{\theta_1})} \tag{5.9}$$

$$\ln \Lambda_2 (r(t)) = \frac{p_{r|H_{\theta_3}}(R|H_{\theta_3})}{p_{r|H_{\theta_1}}(R|H_{\theta_1})} \tag{5.10}$$

$$\ln \Lambda_3 (r(t)) = \frac{p_{r|H_{\theta_4}}(R|H_{\theta_4})}{p_{r|H_{\theta_1}}(R|H_{\theta_1})} \tag{5.11}$$

and so on. Here, R is the v^{th} order representation of $r(t)$ and it can be written as the vector $R = [r_1, r_2, \cdots, r_v]$. The decision regions in the decision space are determined by the the threshold comparisons,

$$\ln \Lambda_1 (r(t)) \underset{H_{\theta_2} \text{ or } H_3}{\overset{H_{\theta_1} \text{ or } H_{\theta_3}}{\gtrless}} \ln \frac{P_1}{P_2} \tag{5.12}$$

$$\ln \Lambda_2 (r(t)) \underset{H_{\theta_3} \text{ or } H_{\theta_2}}{\overset{H_{\theta_1} \text{ or } H_{\theta_2}}{\gtrless}} \ln \frac{P_1}{P_3} \tag{5.13}$$

$$\ln \Lambda_2 (r(t)) \underset{H_{\theta_3} \text{ or } H_{\theta_1}}{\overset{H_{\theta_2} \text{ or } H_{\theta_1}}{\gtrless}} \ln \Lambda_1 (r(t)) + \ln \frac{P_2}{P_3} \tag{5.14}$$

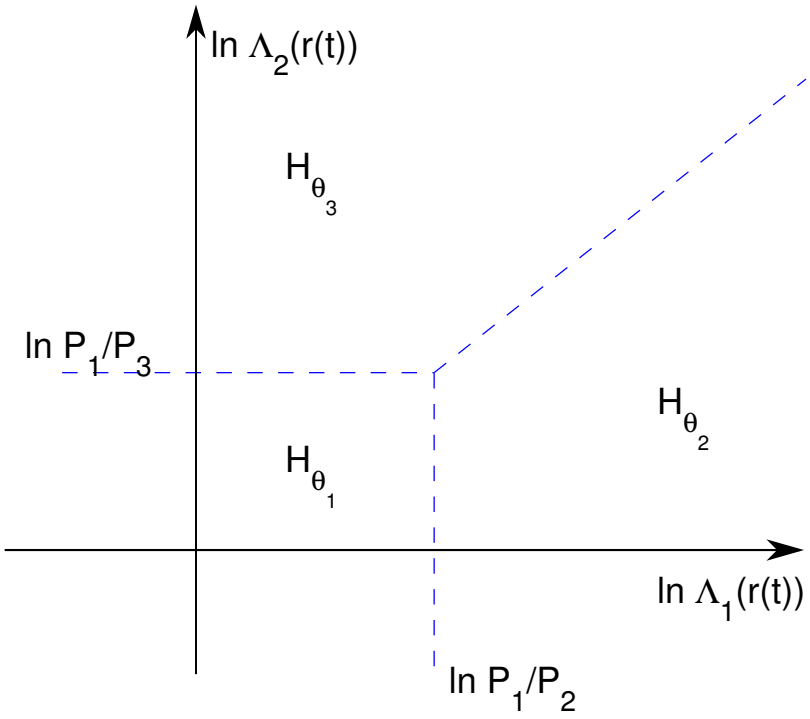

Figure 5.17: Decision Space divided into three detection regions

In figure 5.17, if $P_{\theta_1} = P_{\theta_2} = P_{\theta_3} = \frac{1}{3}$, the dividing line between regions H_{θ_1} and H_{θ_2} will be the negative x-axis and the dividing region between H_{θ_2} and H_{θ_3} will

be the $y = x, x \geq 0$ line and the dividing line between H_{θ_3} and H_{θ_1} will be negative y-axis. In this case we assume that the $P_{\theta_1} = P_{\theta_2} = P_{\theta_3} = \frac{1}{3}$.

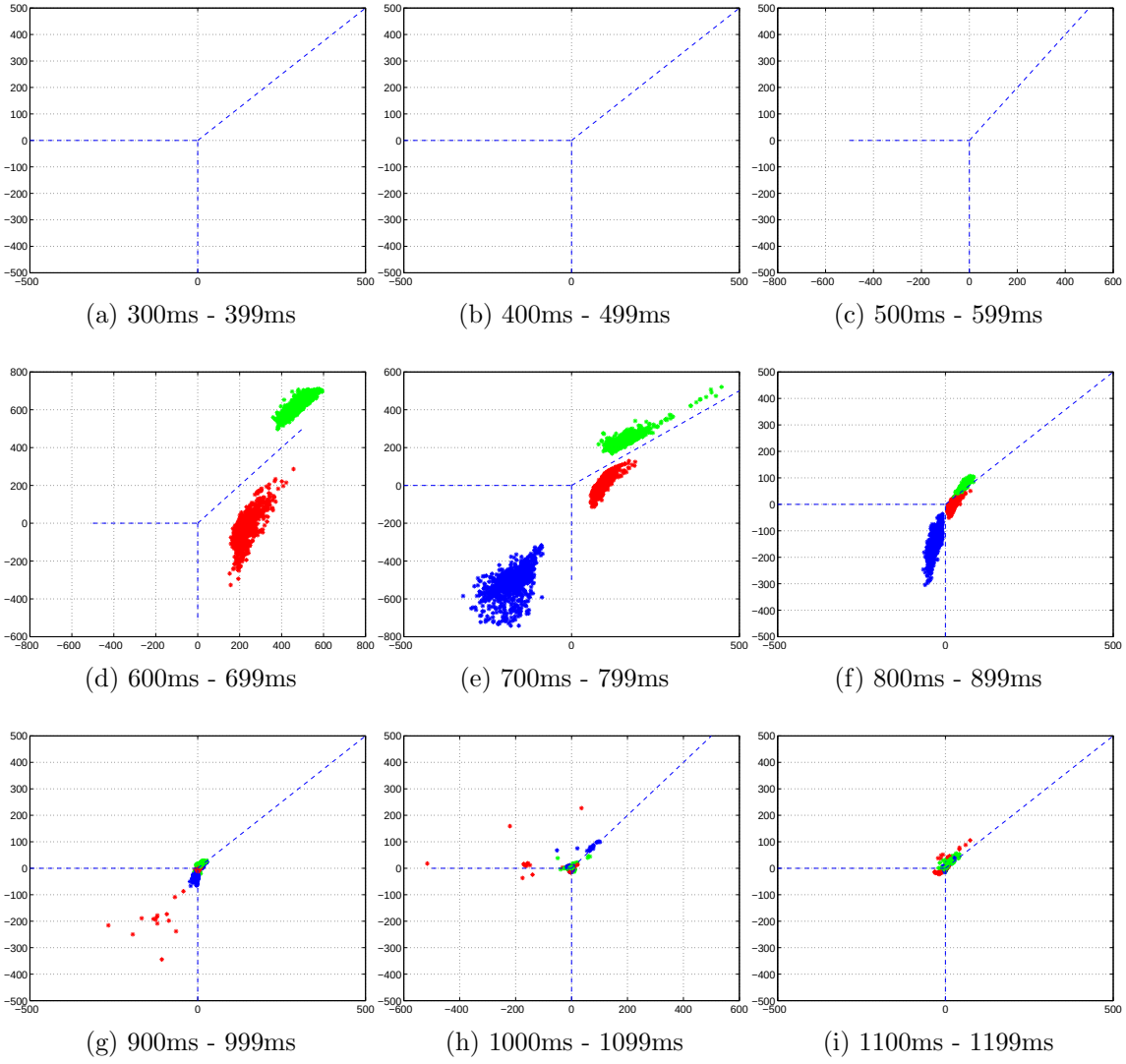

(a) 300ms - 399ms (b) 400ms - 499ms (c) 500ms - 599ms

(d) 600ms - 699ms (e) 700ms - 799ms (f) 800ms - 899ms

(g) 900ms - 999ms (h) 1000ms - 1099ms (i) 1100ms - 1199ms

Figure 5.18: Decision space for motion targets $0°, 30°$ and $60°$, 300-1100ms

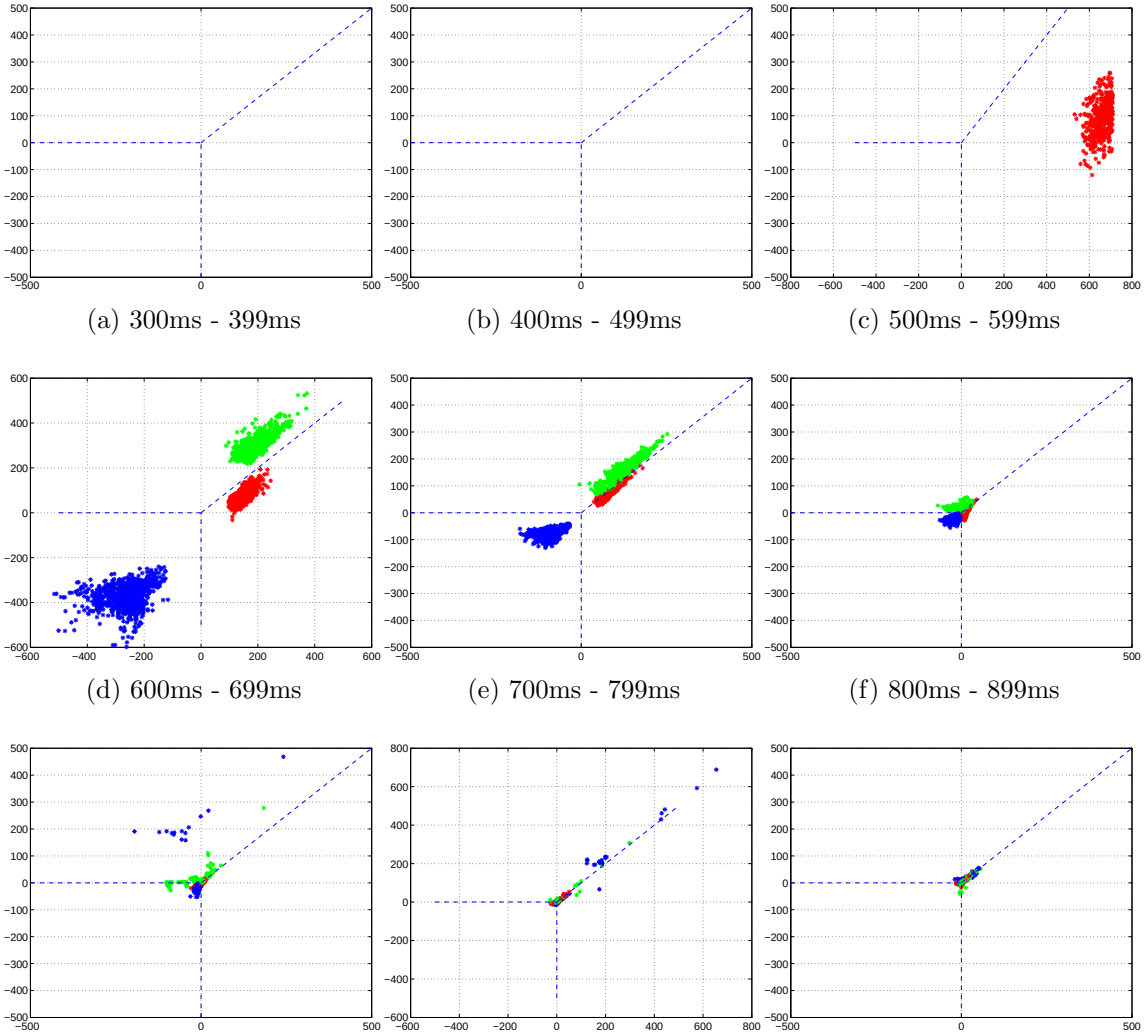

(a) 300ms - 399ms (b) 400ms - 499ms (c) 500ms - 599ms

(d) 600ms - 699ms (e) 700ms - 799ms (f) 800ms - 899ms

(g) 900ms - 999ms (h) 1000ms - 1099ms (i) 1100ms - 1199ms

Figure 5.19: Decision space for motion targets $30°, 60°$ and $90°$, 300-1100ms

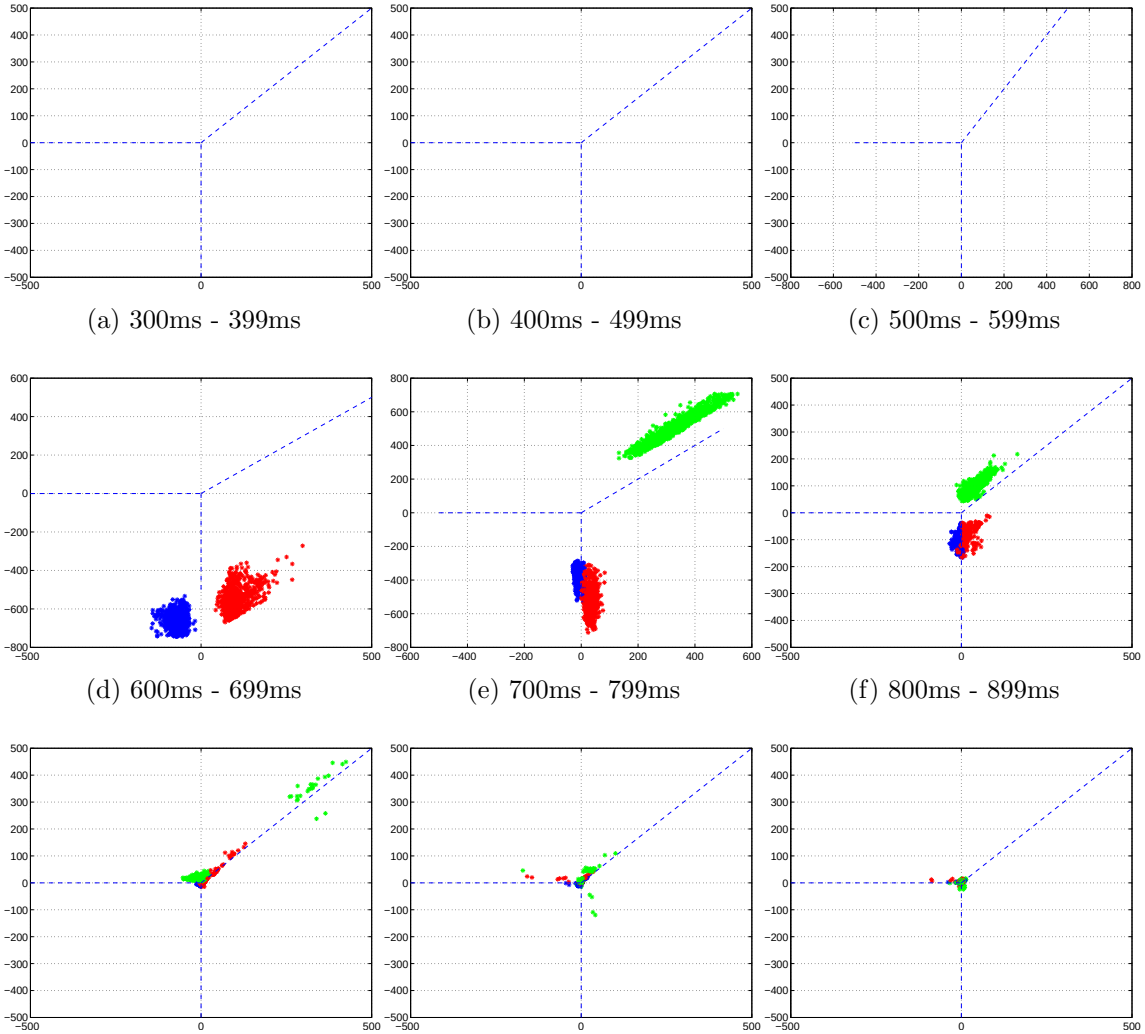

(a) 300ms - 399ms (b) 400ms - 499ms (c) 500ms - 599ms

(d) 600ms - 699ms (e) 700ms - 799ms (f) 800ms - 899ms

(g) 900ms - 999ms (h) 1000ms - 1099ms (i) 1100ms - 1199ms

Figure 5.20: Decision space for motion targets $60°, 90°$ and $120°$, 300-1100ms

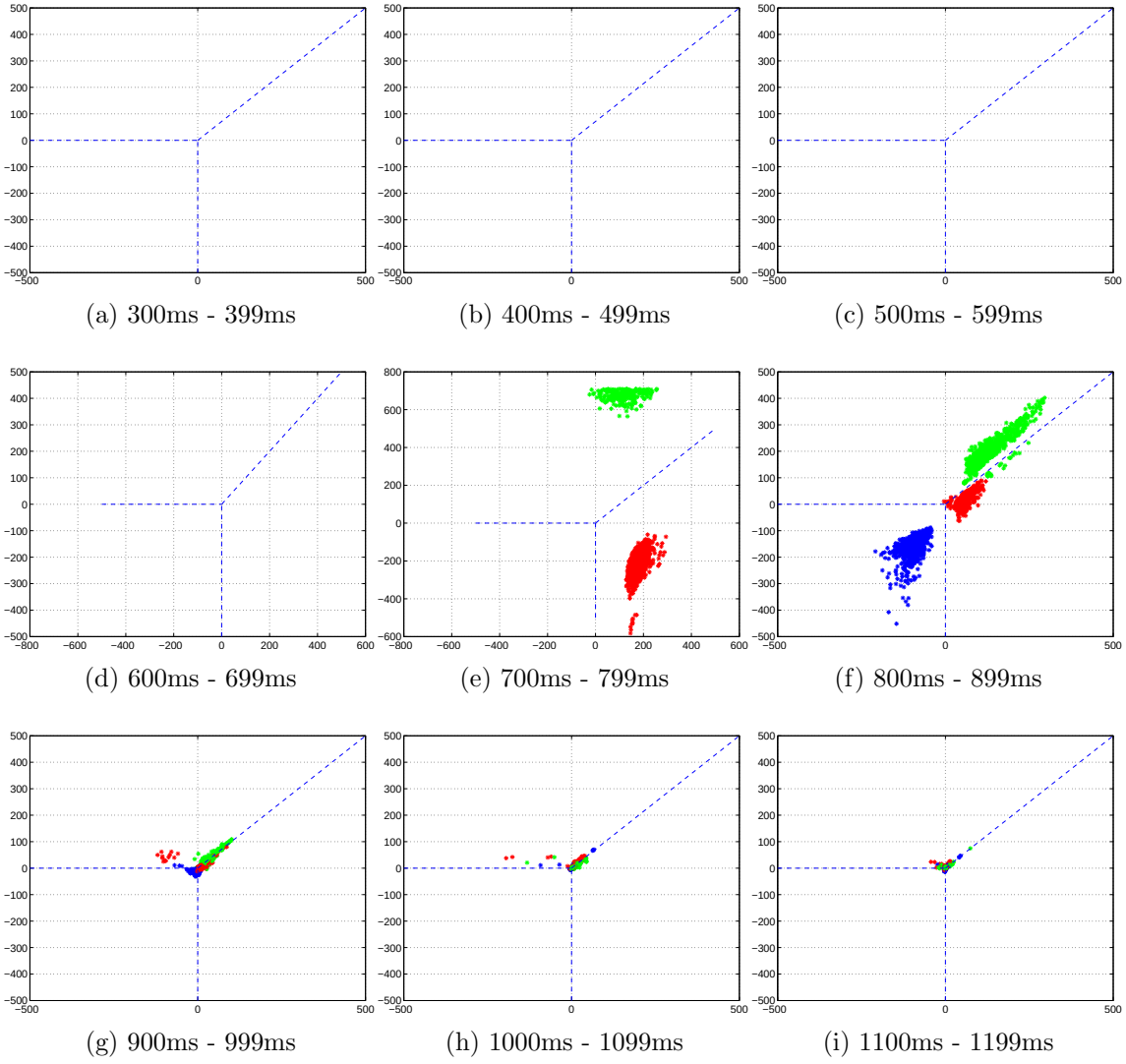

(a) 300ms - 399ms (b) 400ms - 499ms (c) 500ms - 599ms

(d) 600ms - 699ms (e) 700ms - 799ms (f) 800ms - 899ms

(g) 900ms - 999ms (h) 1000ms - 1099ms (i) 1100ms - 1199ms

Figure 5.21: Decision space for motion targets $90°, 120°$ and $150°$, 300-1100ms

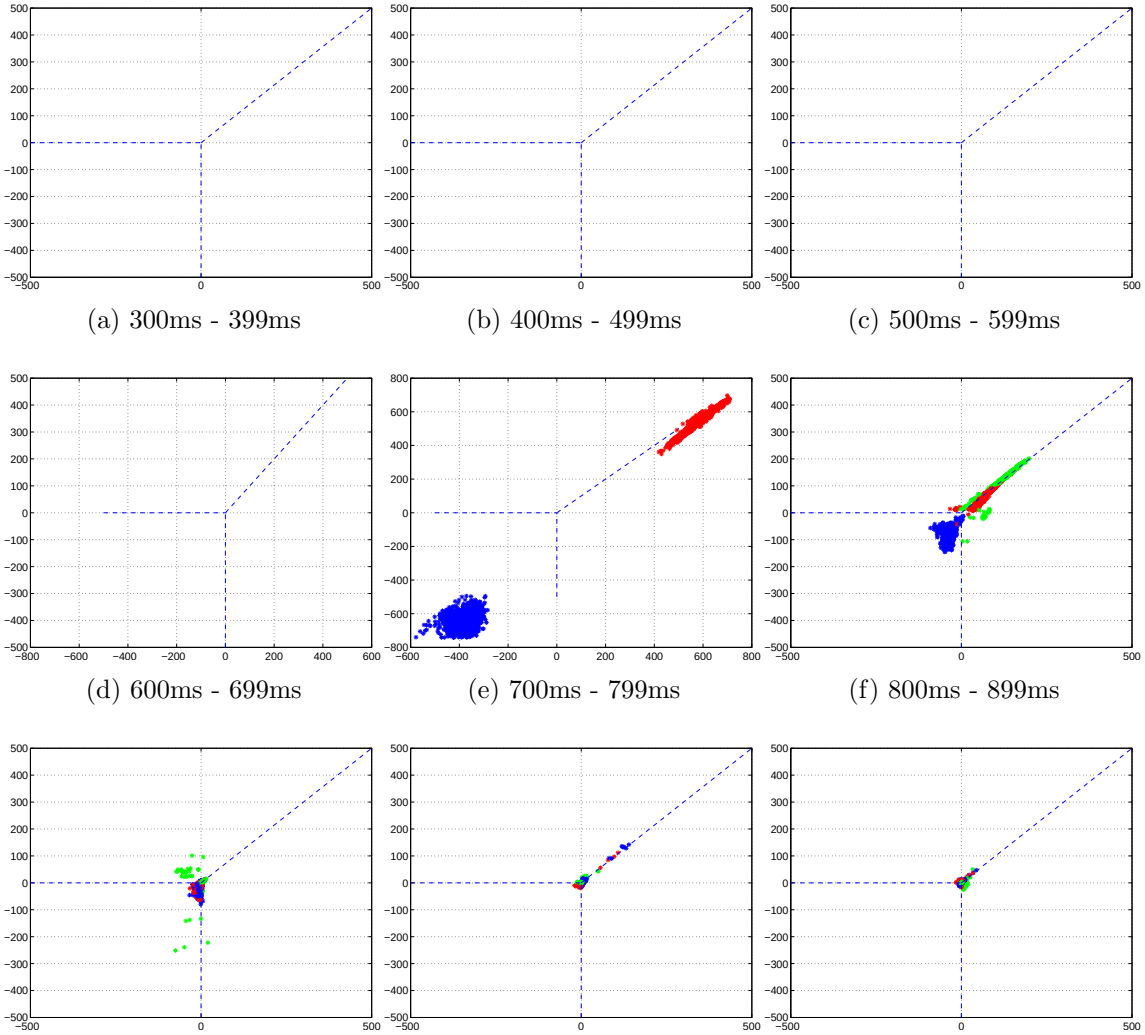

(a) 300ms - 399ms (b) 400ms - 499ms (c) 500ms - 599ms

(d) 600ms - 699ms (e) 700ms - 799ms (f) 800ms - 899ms

(g) 900ms - 999ms (h) 1000ms - 1099ms (i) 1100ms - 1199ms

Figure 5.22: Decision space for motion targets $120°, 150°$ and $180°$, 300-1100ms

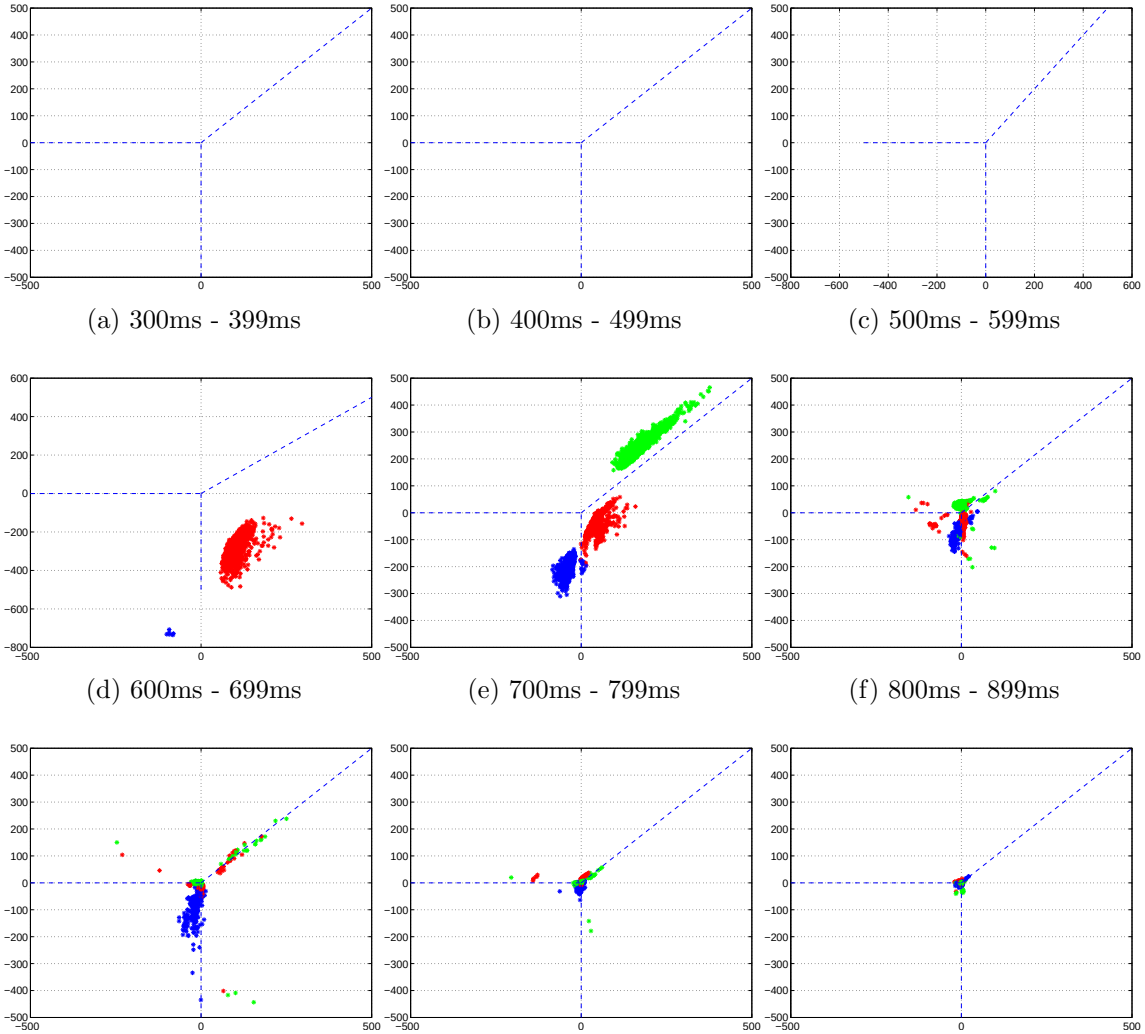

(a) 300ms - 399ms (b) 400ms - 499ms (c) 500ms - 599ms

(d) 600ms - 699ms (e) 700ms - 799ms (f) 800ms - 899ms

(g) 900ms - 999ms (h) 1000ms - 1099ms (i) 1100ms - 1199ms

Figure 5.23: Decision space for motion targets $150°, 180°$ and $210°$, 300-1100ms

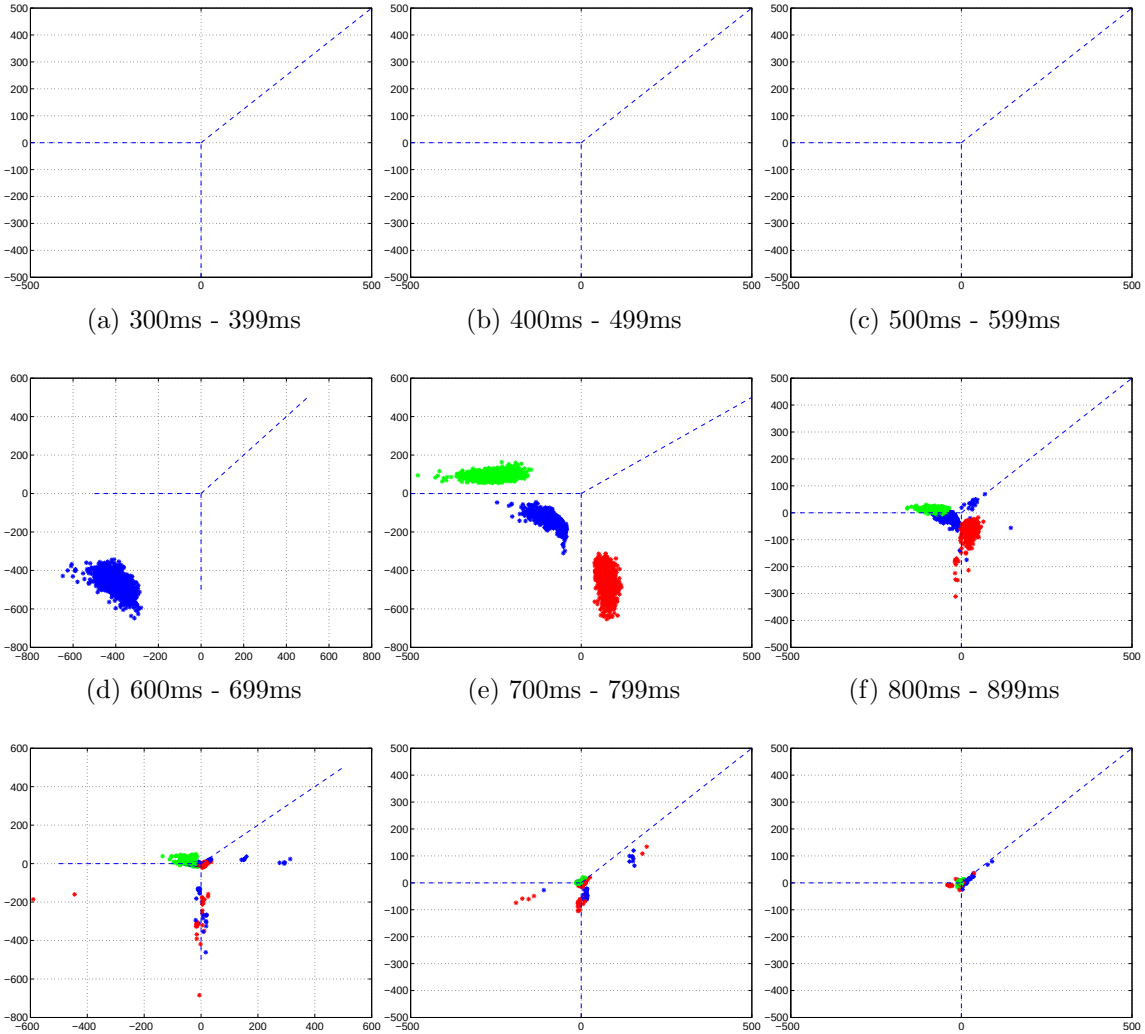

(a) 300ms - 399ms (b) 400ms - 499ms (c) 500ms - 599ms

(d) 600ms - 699ms (e) 700ms - 799ms (f) 800ms - 899ms

(g) 900ms - 999ms (h) 1000ms - 1099ms (i) 1100ms - 1199ms

Figure 5.24: Decision space for motion targets $180°, 210°$ and $240°$, 300-1100ms

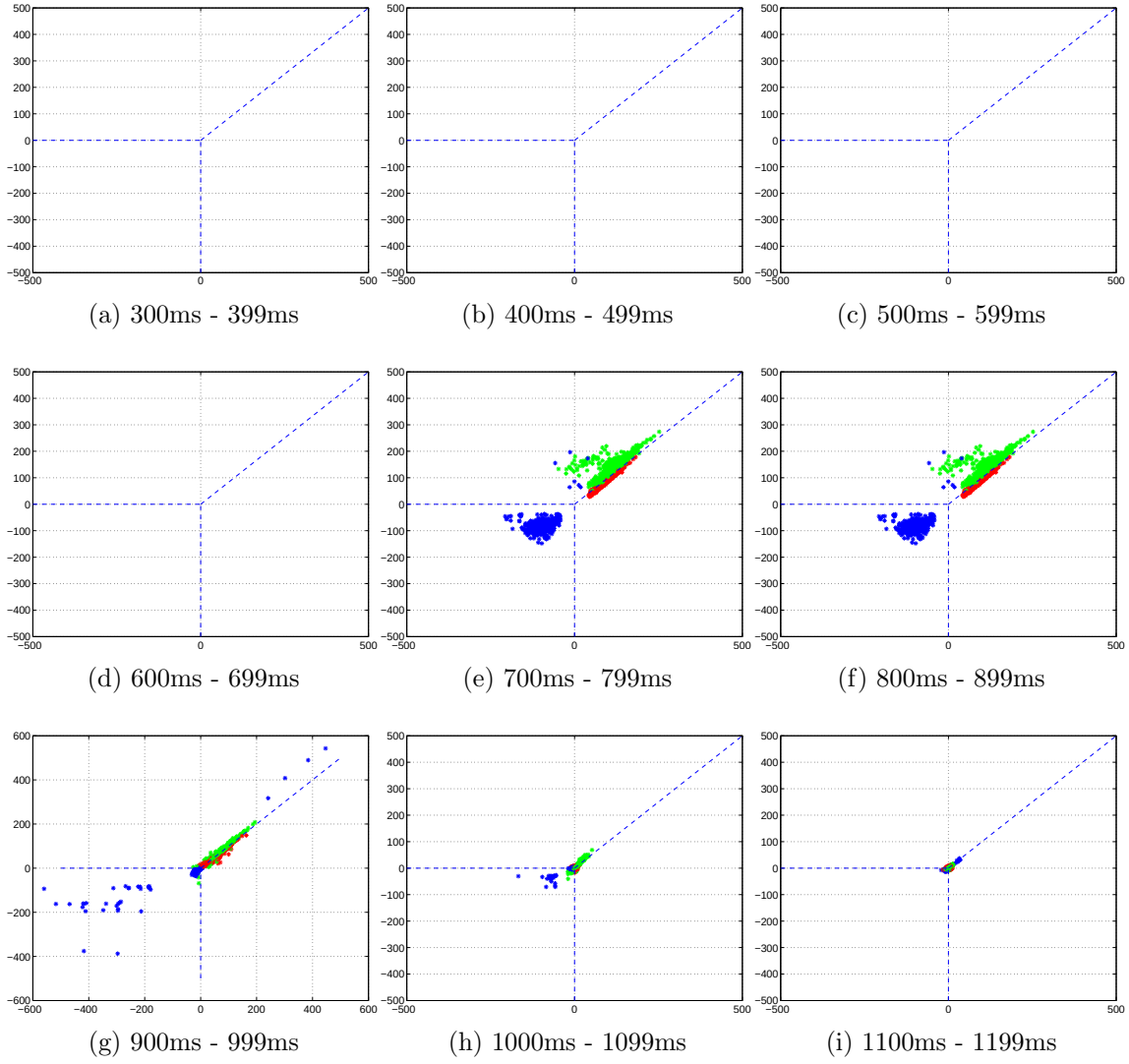

(a) 300ms - 399ms (b) 400ms - 499ms (c) 500ms - 599ms

(d) 600ms - 699ms (e) 700ms - 799ms (f) 800ms - 899ms

(g) 900ms - 999ms (h) 1000ms - 1099ms (i) 1100ms - 1199ms

Figure 5.25: Decision space for motion targets $210°, 240°$ and $270°$, 300-1100ms

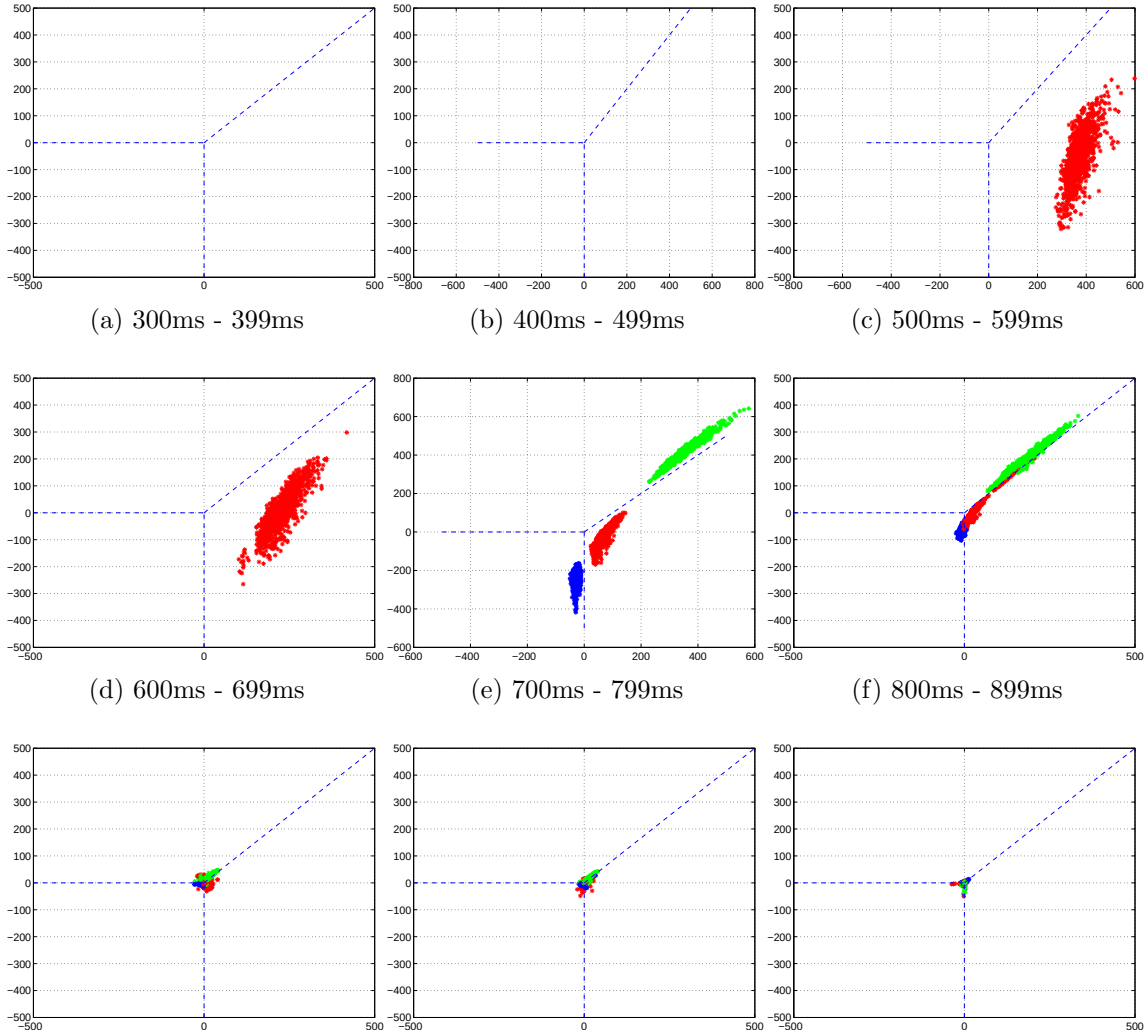

(a) 300ms - 399ms (b) 400ms - 499ms (c) 500ms - 599ms

(d) 600ms - 699ms (e) 700ms - 799ms (f) 800ms - 899ms

(g) 900ms - 999ms (h) 1000ms - 1099ms (i) 1100ms - 1199ms

Figure 5.26: Decision space for motion targets $240°, 270°$ and $300°$, 300-1100ms

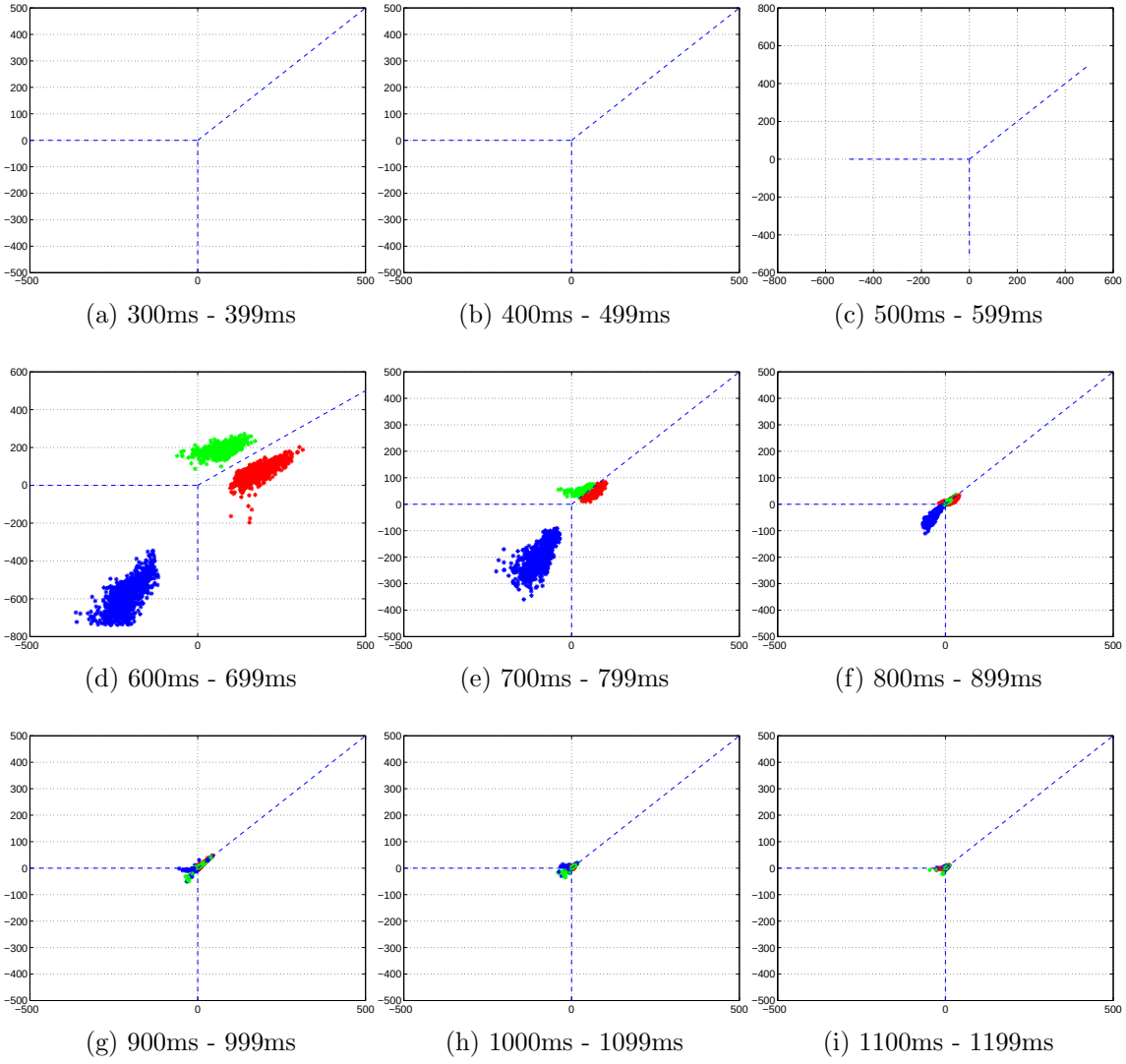

(a) 300ms - 399ms (b) 400ms - 499ms (c) 500ms - 599ms

(d) 600ms - 699ms (e) 700ms - 799ms (f) 800ms - 899ms

(g) 900ms - 999ms (h) 1000ms - 1099ms (i) 1100ms - 1199ms

Figure 5.27: Decision space for motion targets $270°, 300°$ and $330°$, 300-1100ms

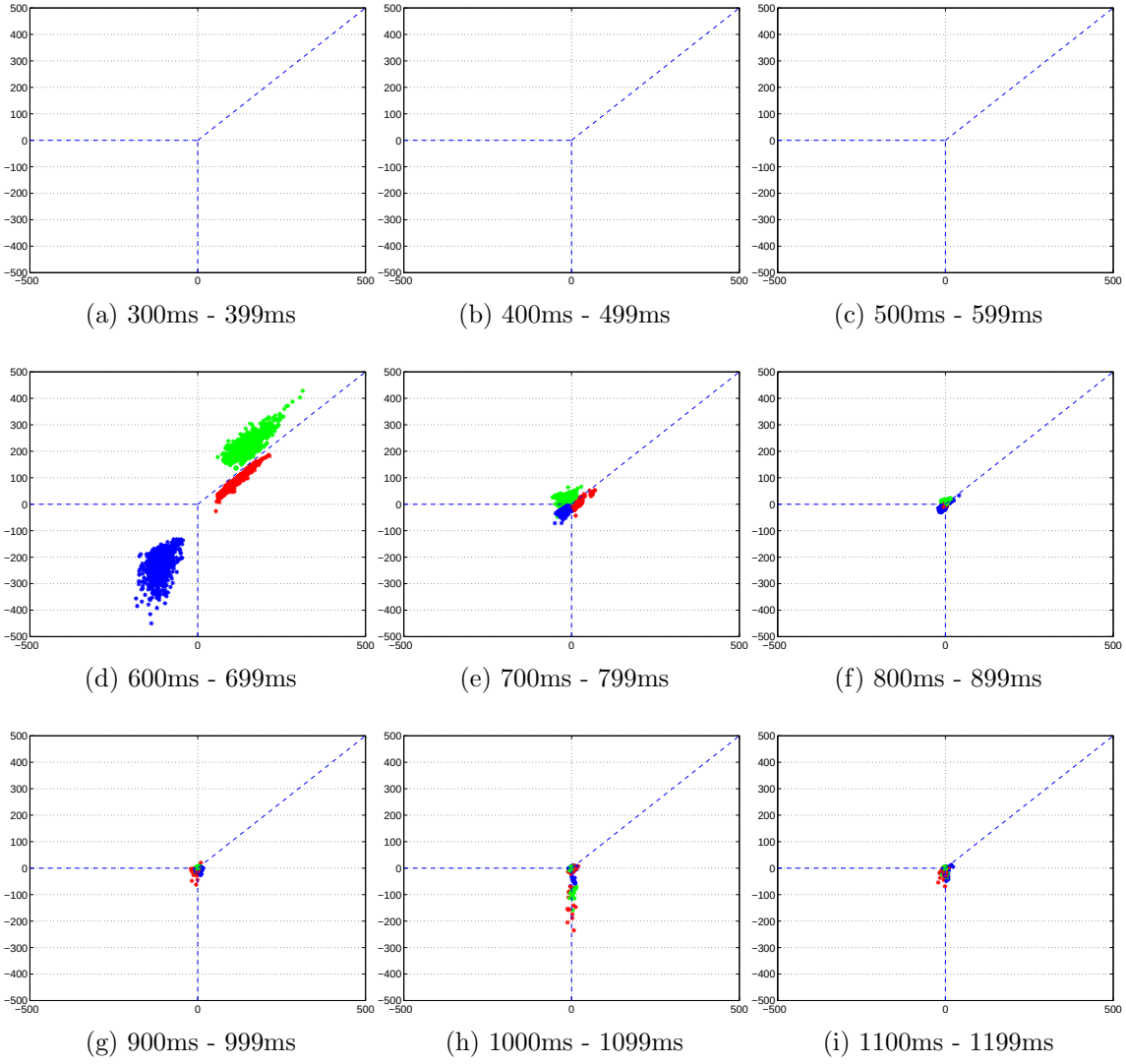

(a) 300ms - 399ms (b) 400ms - 499ms (c) 500ms - 599ms

(d) 600ms - 699ms (e) 700ms - 799ms (f) 800ms - 899ms

(g) 900ms - 999ms (h) 1000ms - 1099ms (i) 1100ms - 1199ms

Figure 5.28: Decision space for motion targets $300°, 330°$ and $0°$, 300-1100ms

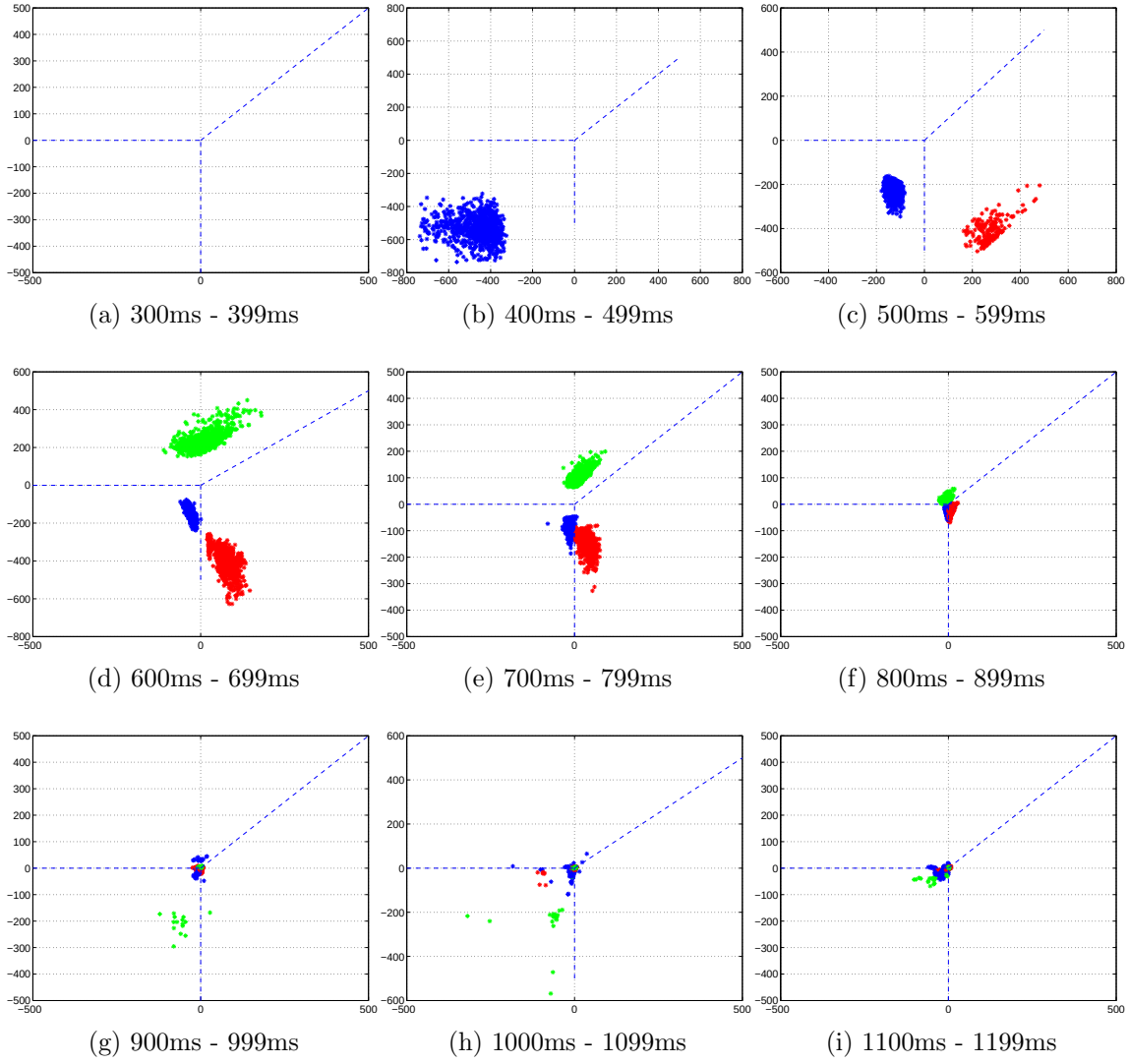

(a) 300ms - 399ms (b) 400ms - 499ms (c) 500ms - 599ms

(d) 600ms - 699ms (e) 700ms - 799ms (f) 800ms - 899ms

(g) 900ms - 999ms (h) 1000ms - 1099ms (i) 1100ms - 1199ms

Figure 5.29: Decision space for motion targets $330°, 0°$ and $30°$, 300-1100ms

CHAPTER VI
RESULTS AND CONCLUSION

Turtle's visual cortex model has shown that it can be used to discriminate stimuli given to it successfully. Also, the retina model has been used successfully to discriminate motion targets and even different motion speeds. In this thesis, we have combined the retinal model and the visual cortex model and the retinal model was used to provide stimuli to the visual cortex model in real time. It was discovered that the combined model of retina and visual cortex can be used to discriminate visual targets successfully.

Another important observation made in this experiment was that the two models should be connected dynamically with connection weights adjusting after the models get stabilized. If the two models connects from the beginning with full connection strength, the expected results could not obtain and the model shows visual cortex activities even without any input stimuli to the retina depending on the connection strength between the retina and the visual corex.

The white noise level plays a key role in statistical analysis, specially in hypothesis testing. If there is no significant white noise in the model, the hypothesis testing fails. It there is too much white noise, the model tend to fire neurons prematurely and expected results cannot be obtained.

BIBLIOGRAPHY

[1] D. B. Bowling. Light responses of ganglion cells in the retina of the turtle. *Journal of Physiology*, 299:173–196, February 1980.

[2] J. E. Dowling. *The Retina: An Approachable Part of the Brain*. Belknap Press of the Harvard University Press, Cambridge, MA, 1987.

[3] X. Du, B. K. Ghosh, and P. S. Ulinski. Encoding and decoding target locations with waves in the turtle visual cortex. *IEEE Transactions in Biomedical Engineering*, 52(4):566–577, April 2005.

[4] M. P. B. Ekanayake. *Motion Encoding and Decoding in the Turtle Retina*. PhD thesis, Department of Mathematics and Statistics, Texas Tech University, Lubbock, TX 79409, USA, July 2011.

[5] A. L. Hodgkin and A. F. Huxley. A quantitative description of membrane current and its application to conduction and excitation in nerve. *Journal of Physiology*, 117:500–544, 1952.

[6] I. T. Jolliffe. *Principal Component Analysis*. Springer Series in Statistics. Springer, New York, NY, 2nd edition, 2002.

[7] Z. Nenadic and B. K. Ghosh. Signal processing and control problems in the brain. *IEEE Control Systems Magazine*, pages 28–41, August 2001.

[8] Z. Nenadic, B. K. Ghosh, and P. S. Ulinski. Modeling and estimation problems in the turtle visual cortex. *IEEE Transactions in Biomedical Engineering*, 49(8):753–762, August 2002.

[9] Z. Nenadic, B. K. Ghosh, and P. S. Ulinski. Propagating waves in visual cortex: A large scale model of the visual cortex. *Journal of Computational Neuroscience*, 14:161–184, 2003.

[10] NewAuthor1 and K. A. Robbins. High-speed vsd imaging of visually evoked cortical waves: Decomposition into intra- and intercortical wave motions. *Journal of Neurophysiology*, 87:1499–1514, 2002.

[11] J. C. Prechtl. Visual motion induces synchronous oscillations in turtle visual cortex. In *Proceedings of the National Academy of Sciences of the United States of America*, volume 91, pages 12467–12471. National Academy of Sciences, 1994.

[12] J. C. Prechtl, T. H. Bullock, and D. Kleinfeld. Direct evidence for local oscillatory current sources and intracortical phase gradients in turtle visual cortex. In *Proceedings of the National Academy of Sciences of the United States of America*, volume 97, pages 877–882. National Academy of Sciences, 2000.

[13] J. C. Prechtl, L. B. Cohen, P. P. Mitra, B. Pesaran, and D. Kleinfeld. Visual stimuli induce waves in electrical activity in turtle cortex. In *Proceedings of the National Academy of Sciences of the United States of America*, volume 94, pages 7621–7626. National Academy of Sciences, 1997.

[14] R. D. Rodieck. *The First Steps in Seeing*. Sinauer, Sunderland, MA, 1998.

[15] D. M. Senseman. Correspondence between visually evoked voltage-sensitive dye signals and synaptic activity recorded in cortical pyramidal cells with intracellular microelectrodes. *Visual Neuroscience*, 13:963–977, 1996.

[16] D. M. Senseman. Spatiotemporal structure of depolarization spread in cortical pyramidal cell populations evoked by diffuse retinal light flashes. *Visual Neuroscience*, 16:65–79, 1999.

[17] D. M. Senseman and K. A. Robbins. Modal behavior of cortical neural networks during visual processing. *Journal of Neuroscience*, 19:RC3(1–7), 1999.

[18] P. S. Ulinski. The cerebral cortex in reptiles. In E. G. Jones and A. Peters, editors, *Cerebral Cortex. Vol. 8A, Comparative Structure and Evolution of Cerebral Cortex, Part I*, pages 139–215. Plenum Press, New York, NY, 1990.

[19] P. S. Ulinski. Neural mechanisms underlying the analysis of moving visual stimuli. In P. S. Ulinski, E. G. Jones, and A. Peters, editors, *Cerebral Cortex. Vol. 13. Models of Cortical Circuitry*, pages 283–399. Plenum Press, New York, NY, 1999.

[20] H. L. Van Trees. *Detection, Estimation and Modulation Theory, Part I.* John Wiley & Sons Inc., New York, NY, 1968.